Journal of Spacecraft and Rockets, Available online 19 May 2025
DOI:10.2514/1.a36092

# Wind Tunnel Installation Effects on a High-Speed Exhaust Flow under Large Blockage

Spyros Tsentis*, Ioannis Goulos†, Marco Debiasi‡, Simon Prince§ and Vassilios Pachidis¶
*Cranfield University, Bedford, United Kingdom, MK43 0AL*

Vladeta Zmijanovic‖
*Reaction Engines Ltd., Oxford, United Kingdom, OX14 3DB*

Josè Saavedra**
*Rolls-Royce Plc., Bristol, United Kingdom, BS34 7QE*

**This study presents a numerical investigation of wind tunnel installation effects on the exhaust flow for a high-speed system under a blockage ratio of 16.5%. The configuration features a nozzle and a cavity embedded at the base of an ogive-cylindrical body, and is representative of future, high-speed exhausts. The work is motivated by the need of testing relatively large, powered-on models and the size of most closed transonic tunnels available in academic research facilities. This combination leads to high blockage ratios and therefore, severe flow distortion. The objective is to examine the installation effects and quantify the level of base flow similarity to unbounded conditions. The employed numerical approach is validated against experimental data. A jet vectoring effect is identified as a result of the presence of the pylon, which is intensified under choked tunnel operation. Additionally, a methodology is proposed which allows base pressure to be compared to unbounded flow conditions. Results show that the pressure distribution agrees within 1.5% and 0.1% for the base and cavity walls, respectively. This demonstrates that local aerodynamic similarity can be established between large-blockage, tunnel-tested conditions and unbounded flow through the proposed approach. This enables the use of small-scale facilities for base flow studies of high-speed exhausts under large blockage.**

## I. Nomenclature

$a_j$ = jet deflection angle, deg

A version of this paper was presented at the AIAA SciTech 2024 Forum, Orlando, Florida, 08-12 January, with paper number AIAA 2024-1774
*Ph.D. Student, Centre for Propulsion and Thermal Power Engineering, Cranfield University, corresponding author, spyros.tsentis@cranfield.ac.uk
†Senior Lecturer in Propulsion Aerodynamics and Performance Engineering, Centre for Propulsion and Thermal Power Engineering, Cranfield University, i.goulos@cranfield.ac.uk
‡Research Fellow, Aeromechanical Systems Group, Centre for Defence Engineering, Cranfield University, marco.debiasi@cranfield.ac.uk
§Professor of Aerodynamics, Centre for Aeronautics, Cranfield University, simon.prince@cranfield.ac.uk
¶Professor and Head of Centre for Propulsion and Thermal Power Engineering, Cranfield University, v.pachidis@cranfield.ac.uk
‖Senior Aerothermal Engineer, Reaction Engines Ltd., vladeta.zmijanovic@polytechnique.edu
**Aerothermal Systems Engineer, Rolls-Royce Plc., jose.saavedra@rolls-royce.com

Published by AIAA. This is the Author Accepted Manuscript issued with: Creative Commons Attribution Non-Commercial License (CC:BY:NC 4.0).
The final published version (version of record) is available online at DOI:10.2514/1.a36092. Please refer to any applicable publisher terms of use.

$c_p$ = specific heat at constant pressure, J/(kg · K)

$C_{V,s}$ = nozzle standard velocity coefficient

$D$ = model diameter, m

$F_G^x$ = axial gauge stream force, N

$F_{G,s}$ = standard gross thrust, N

$k$ = turbulent kinetic energy, $m^2/s^2$

$L$ = model length, m

$M_a$ = wind tunnel approach Mach number

$M_{aft}^{eff}$ = effective Mach number at the end of the afterbody

$M_\infty$ = free-stream Mach number for unbounded flow

$p_{aft}$ = static pressure at the end of the afterbody, Pa

$p_b$ = base static pressure, Pa

$p_{in}$ = wind tunnel inlet static pressure, Pa

$p_{out}$ = wind tunnel outlet static pressure, Pa

$p_w$ = wall static pressure, Pa

$p_\infty$ = free stream static pressure, Pa

$P_{0,n}$ = nozzle inlet total pressure, Pa

$P_{0,t}$ = wind tunnel total pressure, Pa

$R$ = base radius, m

$r$ = radial distance from the axis of symmetry, m

$r_K$ = radial distance of the base pressure sensors, m

$Re_D$ = Reynolds number based on diameter D

$Re_L$ = Reynolds number based on length L

$T$ = static temperature, K

$T_0$ = total temperature, K

$u_x$ = axial velocity component, m/s

$y^+$ = non-dimensional wall distance

$\alpha$ = local surface angle, deg

$\gamma$ = ratio of specific heats

$\Delta\Phi$ = change in variable $\Phi$, %

$\theta$ = fluid force in thrust domain, N

$\lambda$ = thermal conductivity, W/(m · K)

$\mu$ = dynamic viscosity, kg/(m · s)

$\mu_t$ = eddy viscosity, kg/(m · s)

$\rho$ = density, kg/m$^3$

$\tau_w$ = wall shear stress, N/m$^2$

$\phi$ = fluid force in drag domain, N

$\psi$ = azimuthal angle, deg

$\omega$ = specific dissipation rate, s$^{-1}$

*Superscripts*

$\psi$ = refers to the azimuthal angle

$-$ = denotes time-averaged component

$\sim$ = denotes mass-averaged value

# II. Introduction

## A. Background

High-speed propulsion concepts have been studied for many years to enable supersonic flight as well as easier space access. Such concepts are usually related to launch vehicles and rocket-based transportation systems. However, air-breathing propulsion has also been considered for such concepts [1, 2], often utilizing systems which feature no rotating components such as Ramjets [3] and Scramjets [4]. Due to their operating principle being based on ram air compression, Ramjets and Scramjets cannot generate static thrust. This has led to the development of more advanced, combined cycle concepts, comprising Turbine-based [5] and Rocket-based [6] combined cycles (TBCC and RBCC respectively), among others.

Pre-cooled, combined cycle engines is another technology that has received attention for future sustainable, high-speed propulsion. This air-breathing concept incorporates a heat-exchanger to cool down the incoming air prior to compression [1]. This facilitates the extended operational range of the downstream turbomachinery and thus, allows the engine to operate at higher Mach numbers, in contrast with most contemporary air-breathing systems. Several concepts based on this principle have been studied over the years [7] and have been found to exhibit significantly improved efficiency, especially over chemical rocket engines in the case of space access [8, 9]. While the performance advantage is well-established from a thermodynamic point of view, the aerodynamic behavior of these concepts is not yet well understood. Such concepts often feature convergent-divergent (C-D) exhaust nozzles at the base to reach the high speeds required for their designed missions. Due to their implementation, the nozzle is usually embedded within the base. This poses a major difference, in terms of canonical base flow physics, compared to contemporary launch vehicles where

the propulsive nozzle juts out of the base. Additionally, cavity regions are often employed around the nozzle in these concepts to facilitate the overall design of the system, and could potentially further modify their aerodynamic behavior. Consequently, further analysis is required for such concepts to understand the salient flow features at the base.

### B. Base flow characteristics

The flow characteristics at the base region of launch vehicles have a critical effect on their aerodynamic performance. The base pressure, ergo the base drag, is highly dependent on the base geometry, approaching flow conditions, engine operation (on or off), and the state of the propulsive nozzle (i.e., over- or under-expansion). These phenomena have been widely investigated over the years utilizing both experimental and numerical methods. Most of the research effort in the public domain is focused on axisymmetric configurations incorporating blunt-based bodies [10–12] and backward facing steps (BFS) [13–15], due to the axisymmetric topology usually found in space launchers.

Saile et al. [16] examined experimentally the base buffeting of a powered BFS geometry, similar to the European launcher Ariane 5, in the subsonic range ($0.5 < M_\infty < 0.9$). At $M_\infty$=0.8, an exceptionally excited area was identified, in line with the critical side loads condition during the ascent of the launcher as reported by Schwane [17]. Additionally, the effect of the nozzle extension length was investigated later on [18], and was found to affect the base flow unsteadiness. The most unfavorable geometry was observed at $L/D$=0.9, where $D$ denotes the diameter of the main cylindrical body and $L$ the nozzle extension length. Paciorri et al. [14] investigated the base flow with and without a cold propulsive jet for a BFS configuration in the range of $0.18 < M_\infty < 0.43$. They found reduced base pressure due to the aspiration effect for the jet-on case [19]. However, this effect was mitigated by extending the nozzle exit further away from the base, demonstrating the fundamental difference between base-embedded and protruding nozzle configurations.

While axisymmetric BFSs are extensively studied for their simplicity and relevance, more detailed launcher base designs have also been explored. For instance, Meliga and Reijasse [20] investigated the effect of side boosters on the base flow and found that their presence reduced the pressure coefficient in the separated region by a factor of 2 compared to an axisymmetric BFS configuration. Furthermore, Schwane [17] provides numerical and experimental insights into the side loads of the European launchers Ariane 5 and Vega. Axisymmetric BFSs are widely studied due to their representative geometry which serves to examine the base flow physics of protruding nozzle configurations in a canonical sense. However, advanced combined cycle propulsion concepts, such as those mentioned earlier, often feature base-embedded nozzles whose exit is co-planar to the engine's base. This alters the flow physics at the base and near-wake regions [14], thereby rendering BFS configurations no longer representative.

Additionally, these concepts usually employ base-embedded cavities to facilitate their design and in-flight operation, which can further modify their aerodynamic behavior compared to rocket-based systems. Cavity effects arise from the necessity for nozzle gimbaling capabilities, thermal protection for critical components and co-planar, separate-jet exhausts where the secondary exhaust system is inactive. While there have been several previous studies on base

geometry modifications with cavities [21, 22], these are mainly focused on the quantification of their effectiveness as a base drag reduction technique [23–25]. Studies where base-embedded cavities are employed as an integral design aspect of the system, necessary for successful operation, have not been reported in the public domain. However, the significance of such cavities has been demonstrated in previous work [26]. It was found that the presence of the cavity region can result in a notable increase of approximately 12% in the drag coefficient with respect to an identical, non-cavity configuration, as a result of higher base drag. Therefore, further investigation on the base flow of such novel concepts is required using of both numerical and experimental techniques.

### C. Limitations in experimental testing

As discussed previously, a critical condition for launch vehicles, in terms of increased side loads, occurs during transonic flight [16, 17]. Base flow analysis is often facilitated through experimental approaches and wind tunnel testing. Such studies provide important insights into the underlying flow physics at the base as well as useful data sets that can be utilized to perform a validation activity against numerical results [27]. However, there are often practical limitations involved in experimental testing of such configurations, including the size of the test section of most closed transonic wind tunnels found in academic research facilities, which tend to be at the size range of $\sqrt{A}$=0.1-0.25 m as reported by Greenwell [28], where A denotes the test section cross-sectional area. This, along with the relatively large size of the investigated model, usually imposed by instrumentation and necessity for high Reynolds numbers, could lead to large blockage ratios ($BRs$), defined as the area ratio of the largest cross-section of the model and support over that of the test section ($A_{model}/A_{tunnel}$). The required size of the model and support can increase notably in the case of powered-on base flows, due to the requirement of accommodating a secondary flow, thus increasing BR further. As a result, increased wind tunnel installation effects could arise.

These effects include flow interaction phenomena caused by the presence of the tunnel walls and the mounting device of the model [29]. Additionally, at high enough BRs and/or approach Mach numbers, tunnel choking could ultimately occur. These effects can notably modify the flow-field in terms of pressure distribution around the model and hence, negatively affect flow similarity with respect to unbounded flow conditions. The latter refers to scenarios where the flow is not physically constrained, such as by tunnel walls. For a choked tunnel in particular, flow similarity is usually rendered invalid as the flow-field in the unbounded case differs significantly from the one observed in the wind tunnel [30]. Even though there have been successful efforts to intentionally choke the flow in a wind tunnel to simulate Mach 1 conditions around simplified bodies such as a double wedge airfoil [31], tunnel choking is typically undesirable [30].

Wind tunnel installation effects have been traditionally studied by experimenters and theoreticians with the main focus of identifying the impact of tunnel walls and blockage on the aerodynamic characteristics of the investigated model. The confined space of the tunnel test section causes local flow acceleration around the model, which compromises

similarity to unbounded flow conditions. According to the Engineering Sciences Data Unit (ESDU) [32], this effect can be neglected at low speeds for simple bluff bodies with BRs below 1% but becomes notable at higher values (typically above 5%), requiring appreciable corrections.

Several studies have investigated the effects of high blockage on simple bluff body geometries due to their canonical nature and ease of BR modification. For example, Saathoff and Melbourne [33], observed a 15% increase in the mean pressure at a BR of 5% for a short axisymmetric cylinder aligned with the flow, emphasizing the need to minimize blockage effects. Choi and Kwon [34] reported that the aerodynamic behavior of the flow around a square-section bluff body, is minimally affected up to BRs of 10% which was suggested as a maximum value. More recently, Huang et al. [35] examined the blockage effects for rectangular prisms in the range of 4.1% <BR<10.1% and found a considerable impact with a monotonic increase in the mean pressure with increasing BR, concluding that further work is still needed to define a broadly acceptable BR limit. Furthermore, in the automotive industry, blockage ratios below 7.5% are typically suggested before corrections are deemed necessary [36]. In the broader context of experimental aerodynamics, Chanetz et al. [29], suggest that the BR should be kept below 16%, though corrections may be required. Clearly, there is no universally acceptable BR limit, as it depends on various factors, including the examined model geometry, the test facility, the flow conditions and the objectives of the experimental campaign, to name a few.

For more complex, powered-on base geometries, the blockage effects remain largely unexplored. While experimental studies on axisymmetric BFSs with propulsive jets at notable BRs exist, the impact of wind tunnel blockage on the observed results has not been examined. For instance, van Gent et al. [37], performed experiments for a powered-on, axisymmetric BFS under a BR of 6%. The authors acknowledged the non-negligible blockage effects on the results, although these effects were not investigated. A comparable base geometry was studied in [38, 39] under a BR of 5% without accounting for the model's support. Similarly, the impact of blockage on the results was not discussed. In general, there appears to be no well-established consensus on the maximum BR value for these analyses. The BR should be minimized to reduce blockage effects without compromising the model size required to achieve relevant Reynolds numbers and meet experimental constraints related to the test facility, instrumentation, and manufacturing limitations.

Several correction methodologies have been developed to account for blockage effects and are widely used on wind tunnel measurements, especially when integral metrics such as lift and drag coefficients are of primary interest. A comprehensive summary of correction methodologies for several types of wind tunnels can be found in [40, 41] as reported by the Advisory Group for Aerospace Research and Development (AGARD). Whilst essential, application of corrections to experimental data to account for wall interference and blockage effects gets more intricate as the geometry of the model gets more complex [32]. Additionally, correcting the experimental data to produce unbounded flow equivalent results is not always the main objective of an experimental campaign. This is especially true in academic facilities where research on relatively new concepts is being conducted and hence, the understanding of dominant flow features usually has priority over acquiring data that can be corrected for unbounded conditions. A typical example of

this scenario, in the context of base flows, is the investigation of base geometry modifications to assess their base drag reduction capabilities [22]. In this case, the correction of the results becomes less important as the main objective is to examine the potential of a concept as a base drag reduction technique from a flow physics perspective. However, even in this case, severe tunnel installation effects might significantly affect the flow at the base and therefore lead to erroneous or misleading results with respect to unbounded flow conditions. The understanding of these limitations becomes particularly important in the case of university facilities, where transonic closed wind tunnels sit at the lower end of the size range compared to their industrial counterparts [28]. Studies addressing this issue either qualitatively or quantitatively, have not been reported in the public domain.

### D. Scope of present work

This study presents a numerical investigation on the wind tunnel installation effects for a sub-scale, high-speed exhaust system, featuring a cold flow, TIC nozzle along with an axisymmetric cavity region embedded at the base. The examined configuration is representative of future advanced propulsion concepts, usually incorporating base-embedded, C-D nozzles and axisymmetric cavities. Three-dimensional, Favre-averaged Navier-Stokes computations are employed to analyse the flow behavior of the tunnel-installed model. The computational approach is validated against experimental data from a dedicated wind tunnel campaign conducted to support this work, under representative conditions of nozzle over-expansion.

The impact of tunnel pressure ratio ($TPR$) and nozzle pressure ratio ($NPR$) on the exhaust flow is characterized in the range of $1.28 < TPR < 1.79$ and $5 < NPR < 20$, respectively. A direct comparison of the tunnel-installed model to an identical configuration where the effect of the tunnel walls has been removed, reveals the pylon's impact on the exhaust. Additionally, base flow similarity of the tunnel-constrained case against unbounded flow conditions is examined. A methodology is proposed to establish comparability of base pressure between the two cases on the basis of a similarity metric, and its effectiveness is assessed. To the authors' knowledge, the similarity characteristics of base pressure between unbounded and tunnel-constrained conditions under large blockage ratios have not been reported in previous studies for powered-on models. This is critical for base drag analyses of future, high-speed exhausts.

## III. Methodology

### A. Experimental apparatus and investigated cases

This section describes the experimental apparatus used for the validation of the employed computational approach. Specifically, experimental data are used to validate the CFD at representative conditions and are reported in the results section. The experiments were conducted in the closed-circuit, ejector-driven transonic wind tunnel (TSWT) of Cranfield University [42], located at the Defence Academy of the United Kingdom. The facility has a 500 mm-long test section of $HxW$=206x228 mm, and in the current configuration features solid walls without perforation. The flow conditions in

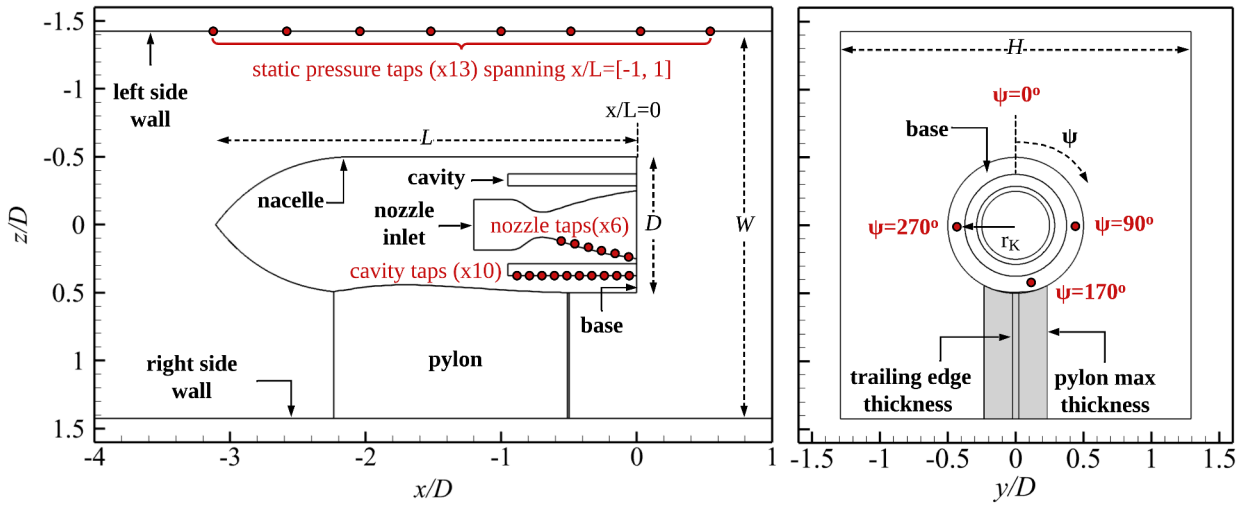


**Fig. 1 Installed exhaust system shown in the x-z (left, top view) and y-z (right, rear view) planes**

the tunnel are controlled by the ejector located downstream of the test section which adjusts its static pressure. The total pressure $P_{0,t}$ of the flow approaching the test section is kept close to the atmospheric value by an atmospheric blow-off box opposite to the test section in the tunnel circuit [42], and is measured by a Druck UNIK 5000 pressure transducer with range from 0.8 to 1.2 bar and accuracy of $\pm 0.4 \cdot 10^{-3}$ bar, connected to a pitot probe in the plenum before the nozzle to the test section. In this study, the tunnel pressure ratio is defined as $TPR=(P_{0,t}/p_{out})$, where $p_{out}$ is the static pressure at the test section outlet. For the empty test section this is essentially the same as $P_{0,t}/p_{in}$, where $p_{in}$ is the reference static pressure from a wall port at the inlet of the test section whose value is measured by a Druck UNIK 5000 pressure transducer with range from 0 to 1 bar and accuracy of $\pm 1 \cdot 10^{-3}$ bar. The signals of $P_{0,t}$ and $p_{in}$ are acquired at a sampling frequency of 100 Hz by the wind tunnel diagnostics. The pressure distribution of the test section after introducing the model is measured by 13 ports equally spaced on the left tunnel wall between the inlet and outlet of the test section, and whose values are obtained by a 32-channel Scanivalve unit (model ZOC 22B/32 Px), with range of 0.31-1.69 bar and accuracy of $\pm 5.5 \cdot 10^{-4}$ bar (8 out of 13 locations are shown in Fig. 1). The Scanivalve signals are acquired at a sampling frequency of 500 Hz for a duration of 20 s which is sufficient to capture the start and stop of the wind tunnel flow. A feed-forward control system regulates the ejector flow required to maintain a prescribed value of $P_{0,t}/p_{in}$ as the pressure decreases in the reservoir tank that drives the tunnel. The corresponding Mach number in the test section remains within ±0.01 of the prescribed value during the approximately 8 s long tunnel discharges.

Figure 1 shows a schematic of the model and tunnel configuration that is numerically investigated in this study in both $x-z$ and $y-z$ planes. Note that the $x-z$ plane is a top view of the model, which is mounted on the right side wall. The model comprises a nacelle surface which is formed by the main cylindrical body and an ogive-shaped nose. It is attached to the right tunnel wall through the pylon which has a NACA 0026 profile cross-section. The maximum pylon thickness and chord, non-dimensionalized over the model's diameter $D$, are approximately 0.46 and 1.77, respectively.

The relatively large size of the pylon is driven by the section required to accommodate the mass flow in the nozzle as dictated by the $NPR$. The dimensions of the tunnel cross-section relative to the model's diameter are approximately equal to $W/D = 2.85$ and $H/D = 2.6$, where $W$ and $H$ are defined in Fig. 1. The model features a high-speed, TIC nozzle embedded at the base. The wall contour of the nozzle in the divergent section is designed using the axisymmetric Method of Characteristics (MoC) [43] to obtain a shock-less flow expansion. Sauer's small perturbation technique [44] is employed at the throat region to approximate the near critical flow conditions and used as an initial-value line for the MoC procedure in the downstream supersonic flow. The resulting ideal nozzle is then truncated at an angle of 7.6 degrees, which corresponds to a design exit Mach number of approximately 3.4 and a design nozzle pressure ratio of $NPR_d$=59. The gray shaded area in the $y-z$ plane view of the model in Fig. 1 corresponds to the maximum thickness of the pylon. The blockage ratio is approximately equal to $(A_{model}/A_{tunnel})$=0.165. Therefore, the impact of tunnel walls and pylon on the exhaust flow must be thoroughly quantified under such large blockage conditions to avoid erroneous results.

Additionally, Fig. 1 shows the experimental locations of the pressure measurements within the model. The expanding flow within the nozzle is monitored with pressure measurements from 6 static ports in the nozzle's divergence, recorded by the Scanivalve unit at a sampling frequency of 500 Hz. Similarly, a total of 10 equally-spaced pressure measurements are collected along the cavity wall normal to the base surface. One RS 797-4961 dynamic pressure transducer with range of 0-25 bar and accuracy of $\pm 2.9 \cdot 10^{-3}$ bar, is used to measure the pressure from a static port in the nozzle inlet. The Mach number at that location can be approximated based on inviscid flow, from the known area ratio of the nozzle inlet and throat sections, and is approximately equal to 0.14. Therefore, the measured pressure is close to the total pressure $P_{0,n}$ within less than 1.4%. This value is actually smaller if the boundary layer build-up is accounted for. Three Kulite XCQ-062-1.7barA miniaturized, dynamic pressure transducers with range of 0-1.7 bar and accuracy of $\pm 1.7 \cdot 10^{-3}$ bar, are used to obtain the pressure at the base of the model. These are located at a radial distance of $r_K = 0.875R$, where $R$ denotes the radius of the base, and at counterclockwise angle locations of approximately 90°, 170° and 270°, with 0° being opposite to the pylon and 180° directly behind it (Fig. 1). Each signal of the Kulite and of the RS transducers is low-pass filtered at 10 kHz by a Dewetron signal-conditioner unit before being acquired at a sampling frequency of 25 kHz. The duration of the corresponding time series is 7.8 s during which the jet is activated for 4 seconds. The maximum measurement uncertainty in the mean values for the static and dynamic pressure measurements based on independent runs was below 2%. This includes all sources of error, such as variation in the approaching flow conditions, variations in the NPR setting and instrumentation noise. The nozzle flow is delivered by a high-pressure air-supply system.

Figure 2 shows the design space in terms of $TPR$ and $NPR$ that is investigated numerically in this study. The exact flow conditions of the CFD test cases are indicated with white circles. Owing to the large blockage ratio, the conditions at the tunnel inlet are strongly dependent on the flow conditions in the vicinity of the model. Therefore, to

avoid ambiguous definition in the design variables, $NPR$ is defined as the ratio between the inlet total pressure of the nozzle $P_{0,n}$, over the outlet static pressure of the tunnel $p_{out}$. Different values of $TPR$ are examined for fixed $NPRs$. As depicted in Fig. 2, this is achieved through the regulation of $P_{0,n}$ and serves to establish orthogonality between $NPR$ and $TPR$. A combination of five different tunnel pressure ratios ($TPR$=1.28, 1.39, 1.52, 1.69, 1.79) and four nozzle pressure ratios ($NPR$=5, 10, 15, 20) are examined, producing a total number of 20 investigated scenarios for the tunnel-installed model.

### B. Performance accounting methodology

The performance accounting methodology of the exhaust system is briefly presented in this section. Leading performance metrics are used to evaluate the discretization error of the computational mesh. Figure 3 illustrates the thrust and drag accounting methodology as employed in this study, which is based on a well-established thrust-drag book-keeping system [45]. A near-field approach is selected to facilitate the direct evaluation of the constituent elements of the total forces. The aerodynamic forces exerted on the wall surfaces of the model and pylon by the fluid flow that reside within the drag and thrust domains are denoted by the symbols $\phi$ and $\theta$, respectively. These aerodynamic forces are obtained through direct numerical integration of the gauge static pressure and shear-stress terms along the wall viscous surfaces, as described in Eq. (1). The gauge stream force $F_G$ as well as the mass flow rate at the nozzle inlet are evaluated through numerical integration at the corresponding boundaries (Eq. (2)).

$$\theta,\ \phi = \iint_S (p - p_\infty) \sin a \, dS + \iint_S t_w \cos a \, dS \tag{1}$$

$$F_G^x = \iint_{Area} \rho u_x^2 dA + \iint_{Area} (p - p_\infty) dA \tag{2}$$

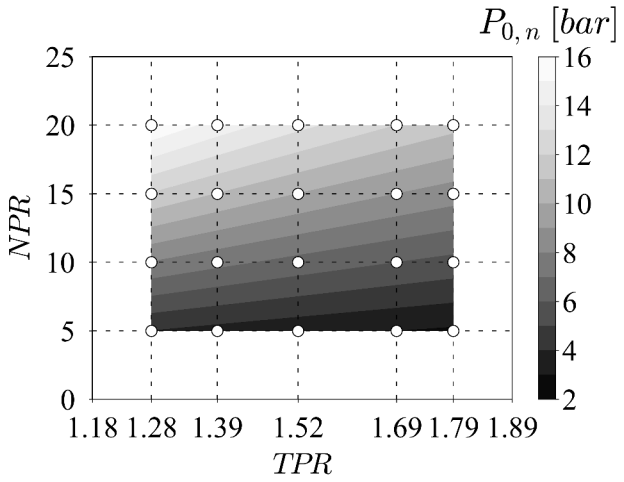


**Fig. 2 Variation of $P_{0,n}$ within the examined design space**

In Eq. (1), $p$ and $\tau_w$ refer to the local static pressure and shear stress respectively, $p_\infty$ refers to the ambient static pressure, here taken at the tunnel outlet, $a$ is the local surface angle measured from the axial direction and $dS$ is the elemental surface area. In Eq. (2), $\rho$ is the density, $u_x$ is the axial velocity component and $dA$ is the elemental surface area of the corresponding boundary.

In order to assess the aerodynamic performance of the exhaust nozzle, the standard velocity coefficient $C_{V,s}$ is used, which represents the ratio of the calculated standard gross thrust $F_{G,s}$, over the ideal thrust (Eq. (3)). The latter, corresponds to the thrust that the system would produce under isentropic, fully-expanded flow to the ambient static pressure. The standard gross thrust is the gauge stream force at the exit of the nozzle and is described in Eq. (4) based on control volume theory. The ideal exit velocity corresponds to the ideal jet exit velocity that would be reached under isentropic expansion to the ambient static pressure and is defined as shown in Eq. (5), where $NPR$ is the nozzle pressure ratio as defined previously, $R$ is the gas constant, $\gamma$ is the ratio of specific heats and $T_0$ is the total temperature at the nozzle inlet. Due to the cases investigated in this study, the nozzle discharge coefficient $C_D$ is not examined, since the nozzle is operating under choked conditions. The summation of the aerodynamic forces that are exerted by the fluid flow on the surfaces and reside within the drag domain, constitute the total modified drag force [45], and is expressed as shown in Eq. (6). Finally, the gross propulsive force ($GPF$), represents the overall aerodynamic force component in the free-stream flow direction which is produced by the exhaust system and is obtained as described by Eq. (7). The $GPF$ allows the overall aerodynamic performance to take into account the regions of separated flow within the nozzle under over-expanded conditions.

$$C_{V,s} = \frac{F_{G,s}}{\dot{m}_{actual}\, V_{ideal}} \tag{3}$$

$$F_{G,s} = F_{G,inlet} - \theta_{nozzle} \tag{4}$$

$$V_{ideal} = \sqrt{\frac{2\gamma R T_0}{(\gamma - 1)} \left(1 - \left(\frac{1}{NPR}\right)^{\frac{\gamma-1}{\gamma}}\right)} \tag{5}$$

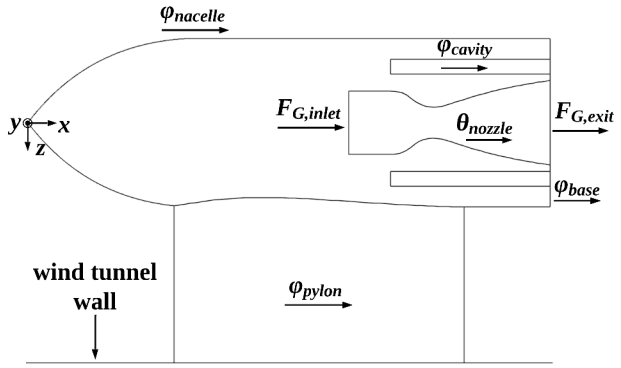


**Fig. 3 Thrust and drag accounting system for the tunnel-installed model**

$$D^* = \phi_{nacelle} + \phi_{base} + \phi_{cavity} + \phi_{pylon} \tag{6}$$

$$GPF = F_{G,s} - D^* \tag{7}$$

### C. Computational approach

*1. Physical model*

The field variables are obtained through the solution of the Favre-averaged version of the three-dimensional Navier-Stokes equations describing the conservation of mass, momentum and energy (Eqs. (8)- (10)) [46]:

$$\frac{\partial \bar{\rho}}{\partial t} + \frac{\partial}{\partial x_i}(\bar{\rho}\tilde{u}_i) = 0 \tag{8}$$

$$\frac{\partial}{\partial t}(\bar{\rho}\tilde{u}_i) + \frac{\partial}{\partial x_j}(\bar{\rho}\tilde{u}_j\tilde{u}_i) + \frac{\partial \bar{p}}{\partial x_i} - \frac{\partial}{\partial x_j}(\bar{t}_{ij} + \bar{\rho}\tau_{ij}) = 0 \tag{9}$$

$$\frac{\partial}{\partial t}(\bar{\rho}E) + \frac{\partial}{\partial x_j}(\bar{\rho}\tilde{u}_j H) - \frac{\partial}{\partial x_j}\left[\tilde{u}_i(\bar{t}_{ij} + \bar{\rho}\tau_{ij})\right] - \frac{\partial}{\partial x_j}\left[\left(\frac{\mu}{Pr} + \frac{\mu_t}{Pr_t}\right)\frac{\partial \tilde{h}}{\partial x_j} + (\mu + \sigma_k\mu_t)\frac{\partial k}{\partial x_j}\right] = 0 \tag{10}$$

where $E$ and $H$ are the total energy and total enthalpy, including the kinetic energy of the turbulent fluctuations as $E = \tilde{e} + \frac{1}{2}\tilde{u}_i\tilde{u}_i + k$ and $H = \tilde{h} + \frac{1}{2}\tilde{u}_i\tilde{u}_i + k$, with $e$ and $h$ being the specific internal energy and specific enthalpy, respectively. In the equations above, $\bar{\rho}$ is the time-averaged fluid density and $\tilde{u}_i$ is the mass-averaged velocity component in the $i$th direction. The total stress tensor, is the sum of the viscous stress tensor, denoted as $\bar{t}_{ij}$, and the Favre-averaged, Reylonds stress tensor $\bar{\rho}\tau_{ij}$, which is defined based on the Boussinesq approximation:

$$\bar{t}_{ij} = 2\mu\bar{S}_{ij} \tag{11}$$

$$\bar{\rho}\tau_{ij} = 2\mu_t\bar{S}_{ij} - \frac{2}{3}\bar{\rho}k\delta_{ij} \tag{12}$$

$$\bar{S}_{ij} = S_{ij} - \frac{1}{3}\frac{\partial \tilde{u}_k}{\partial x_k}\delta_{ij} \tag{13}$$

where $S_{ij}$ denotes the mean strain of rate tensor, $\mu$ is the dynamic viscosity, $\mu_t$ is the eddy viscosity, $\delta_{ij}$ is the Kronecker delta, $k$ is the turbulent kinetic energy and $Pr$ and $Pr_t$ denote the laminar and turbulent Prandtl numbers, respectively. Closure is obtained through the implementation of the two-equation, $k-\omega$ shear stress transport (SST) eddy viscosity model, introduced by Menter [47]. The model solves two transport equations for the turbulent kinetic energy $k$ and specific dissipation rate $\omega$ (Eqs. (14), (15)). Its main formulation is briefly repeated here (Eqs. (16)- (24)).

$$\frac{\partial(\bar{\rho}k)}{\partial t} + \frac{\partial(\bar{\rho}\tilde{u}_i k)}{\partial x_i} = \widetilde{P_k} - \beta^*\bar{\rho}k\omega + \frac{\partial}{\partial x_i}\left[(\mu + \sigma_k\mu_t)\frac{\partial k}{\partial x_i}\right] \tag{14}$$

$$\frac{\partial(\bar{\rho}\omega)}{\partial t} + \frac{\partial(\bar{\rho}\tilde{u}_i\omega)}{\partial x_i} = a\bar{\rho}S^2 - \beta\bar{\rho}\omega^2 + \frac{\partial}{\partial x_i}\left[(\mu + \sigma_\omega\mu_t)\frac{\partial\omega}{\partial x_i}\right] + 2(1-F_1)\rho\sigma_{\omega 2}\frac{1}{\omega}\frac{\partial k}{\partial x_j}\frac{\partial\omega}{\partial x_j} \tag{15}$$

In Eq. (14) the production term of turbulent kinetic energy $P_k$ is defined as:

$$P_k = \mu_t\frac{\partial\tilde{u}_i}{\partial x_j}\left(\frac{\partial\tilde{u}_i}{\partial x_j} + \frac{\partial\tilde{u}_j}{\partial x_i}\right) \tag{16}$$

A production limiter is used in the SST formulation of the $k-\omega$ model to prevent the build-up of turbulence in stagnation regions [48]:

$$\widetilde{P_k} = \min(P_k, 10\beta^*\rho k\omega) \tag{17}$$

The turbulent eddy viscosity is defined as:

$$\nu_t = \frac{a_1 k}{\max(a_1\omega, SF_2)} \tag{18}$$

where $S$ is the magnitude of the strain rate tensor and its use instead of vorticity $\Omega$ in the eddy viscosity definition is a slight modification over the original formulation of the $k-\omega$ SST model [48]. The blending function $F_1$ is given by:

$$F_1 = \tanh(arg_1^4) \tag{19}$$

$$arg_1 = \min\left[\max\left(\frac{\sqrt{k}}{\beta^*\omega y}, \frac{500\nu}{y^2\omega}\right), \frac{4\rho\sigma_{\omega 2}k}{CD_{k\omega}y^2}\right] \tag{20}$$

with $y$ being the distance to the nearest wall surface and $CD_{k\omega}$ is the positive portion of the cross-diffusion term appearing in the transport equation of $\omega$, defined as:

$$CD_{k\omega} = \max\left(2\rho\sigma_{\omega 2}\frac{1}{\omega}\frac{\partial k}{\partial x_j}\frac{\partial\omega}{\partial x_j}, 10^{-10}\right) \tag{21}$$

$F_1$ is equal to one inside the boundary layer ($k-\omega$ model) and switches to zero far away from solid surfaces ($k-\epsilon$ model) because of the dependency to $1/y$ or $1/y^2$ in all three terms of Eq. (20). The second blending function $F_2$ appearing in Eq. (18) is defined by:

$$F_2 = \tanh(arg_2^2) \tag{22}$$

$$arg_2 = \max\left[2\frac{\sqrt{k}}{\beta^*\omega y}, \frac{500\nu}{y^2\omega}\right] \tag{23}$$

All model constants are computed by a blend between the corresponding constants of the $k-\epsilon$ and $k-\omega$ model, and are provided below.

$$\begin{gathered}\sigma_{k1}=0.85, \quad \sigma_{\omega 1}=0.5, \quad \beta_1=0.075, \quad a_1=0.31 \\ \sigma_{k2}=1.0, \quad \sigma_{\omega 2}=0.856, \quad \beta_2=0.0828, \quad \beta^*=0.09 \\ \gamma=\frac{\beta}{\beta^*}-\frac{\sigma_\omega \kappa^2}{\sqrt{\beta^*}}, \quad \kappa=0.41\end{gathered} \tag{24}$$

*2. Computational domain and grid generation*

A half-tunnel approach is employed in this study to construct the computational domain, making use of the $x-z$ symmetry plane and thus, drastically reducing the associated computational cost (Fig. 4). The domain replicates the wind tunnel test section and extends downstream of the base at a distance equal to 10 times the total length of the model $L$. Note that the orientation of the test section is rotated in Fig. 4 for visualization purposes and the model is mounted on the right side tunnel wall. The conditions at the tunnel inlet are modelled by applying a pressure inlet boundary condition (BC) on the corresponding surface, with the total pressure and temperature as the prescribed values. The total pressure at the inlet of the domain is set to atmospheric conditions, while total temperature is set to 290 K for all of the computations. At the outlet of the computational domain, a pressure outlet BC is applied, imposing the static pressure value $p_{out}$, which regulates the $TPR$. The total pressure and temperature at the nozzle inlet are defined by applying a

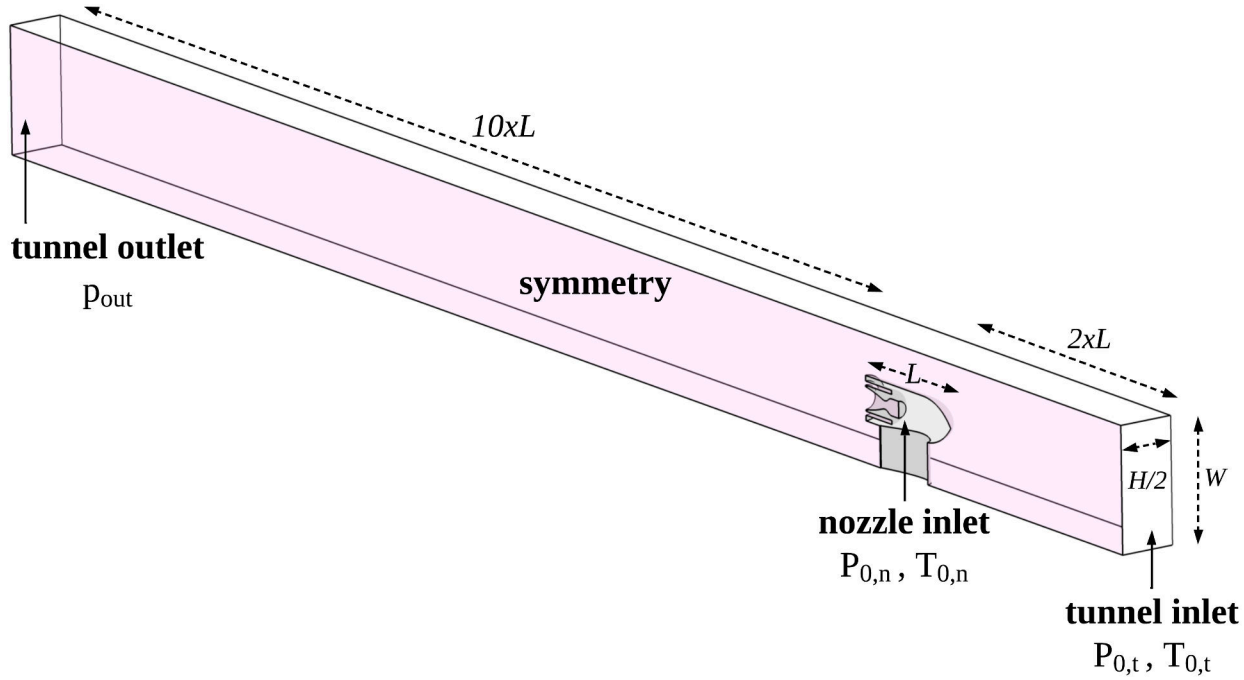


**Fig. 4 Computational domain and boundary conditions**

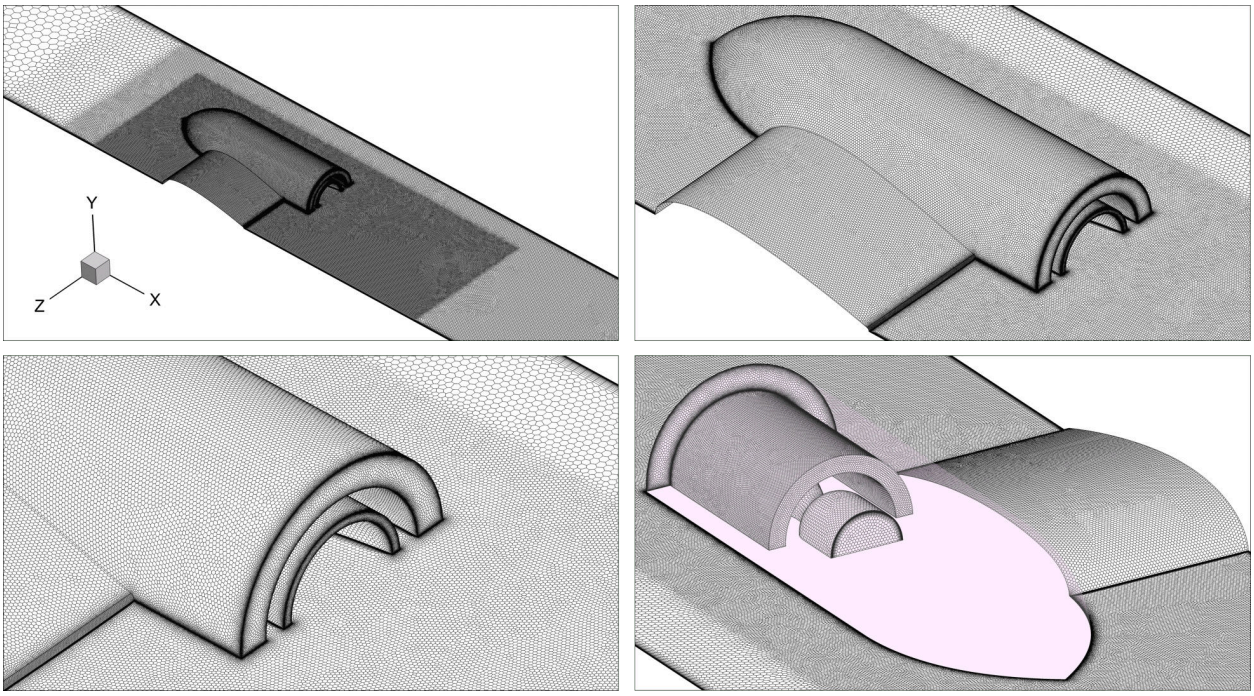


**Fig. 5 Employed surface mesh and close-up views on base and nozzle regions**

pressure inlet BC. Due to the cold-flow nozzle operation in the experiments, the total temperature at the nozzle inlet is fixed at 290 K. The shaded area of Fig. 4 corresponds to the symmetry plane $x - z$ and therefore, a symmetry BC is applied. All of the corresponding surfaces of the model, pylon and tunnel, are modelled as viscous no-slip and adiabatic walls.

A hybrid meshing approach is employed in this study [49]. Figure 5 depicts a close-up view of the derived surface mesh at the base and near-wake regions as well as on the cavity and nozzle. The hybrid approach employs 35 prism layers near the wall surfaces of the model, pylon and tunnel to allow for proper boundary layer resolution. The resulting non-dimensional wall distance, $y^+$ is below 1 for all wall-adjacent nodes. The remainder of the domain is discretized in an unstructured manner, employing polyhedral elements. This type of elements is usually more efficient in terms of cell count compared to tetrahedrons. Additionally, polyhedral elements have been considered in a broad range of aerodynamic flow simulations, including helicopters [50] and buildings [51] among other, and have been found to exhibit similar levels of accuracy as that of more conventional element topologies (e.g., tetrahedrons). Unstructured mesh refinement regions are employed to gradually migrate from the undisturbed flow conditions at the tunnel inlet to the afterbody, base and near-wake regions of the domain, where better resolution is desired (Fig. 5). A cell growth ratio of 1.2 has been maintained throughout the grid generation process. Additionally, the finest grid resolution region extends downstream of the base at a length equal to 12.5 nozzle exit radii.

A grid convergence study was conducted to assess the discretization error, based on the generalized Richardson Extrapolation procedure [52] and using the second order Grid Convergence Index (GCI) [53]. The grid refinement

process was done in a systematic manner by uniformly refining the surface and volume elements based on the local spatial discretization of that region of the mesh, while additional prism layers were added to ensure that consistency with the unstructured grid of the domain is maintained. Therefore, grids comprising 3, 13.7 and 44 million cells were used, providing a grid refinement factor higher than 1.3 as recommended in [53]. A detailed summary of the results of the grid convergence analysis is shown in Table 1 for conditions corresponding to $TPR$=1.28 and $NPR$=20. The investigation of the standard velocity coefficient $C_{V,s}$, allows to evaluate the nozzle operation and efficiency (Eq. (3)), while $GPF$ constitutes an overall metric since it accounts for both the forces exerted on the body as well as the standard gross thrust (Eq. (7)). As shown in Table 1, the GCI corresponding to the medium mesh for the standard velocity coefficient is 0.42%, while the GCI for the $GPF$ is 0.68%. The apparent order $p$, is close to the formal order of the employed discretization scheme ($2^{nd}$), which can be taken as a good indication of the grids being in the asymptotic range [53]. The computational cost of the finest grid is increased by a factor of 5 compared to the medium grid, which translates into an increase by an order of magnitude in the total CPU hours for all computations. Consequently, based on the results of the grid convergence analysis as well as on the computational cost, grids of approximately 13.7 million cells were used.

**Table 1 Calculation of discretization error**

| | $\xi$ = standard velocity coefficient $C_{V,s}$ (monotonic convergence) | $\xi$ = gross propulsive force over $GPF_{fine}$(monotonic convergence) |
|---|---|---|
| N1, N2, N3 | 44M, 13.7M, 3M | 44M, 13.7M, 3M |
| $r_{21}$ | 1.476 | 1.476 |
| $r_{32}$ | 1.647 | 1.647 |
| $\xi_1$ | 0.9501 | 1.0000 |
| $\xi_2$ | 0.9469 | 0.9928 |
| $\xi_3$ | 0.9377 | 0.9681 |
| $p$ | 1.79 | 2.11 |
| $\xi_{ext}^{21}$ | 0.9533 | 1.006 |
| $e_a^{21}$ | 0.34% | 0.72% |
| $e_{ext}^{21}$ | 0.33% | 0.54% |
| $GCI_{fine}^{21}$ | 0.42% | 0.68% |

*3. Description of numerical method*

Computations used an implicit, density-based and compressible Favre-averaged Navier-Stokes solver [54], coupled with the $k-\omega$ SST turbulence model [47], which has been found to perform reasonably well for over-expanded nozzle flow cases [55] as well as for powered-on, afterbody flows with separation [56]. Roe's approximate Riemann solver was used for the calculation of the convective fluxes [57]. Due to the polyhedral topology of the grid, a Green-Gauss cell-based method was employed to calculate the flow-field gradients, to avoid the increased computational cost of a

node-based approach [54]. A second-order accurate upwind scheme was used for discretization of the flow primitive variables as well as for turbulent kinetic energy $k$ and specific dissipation rate $\omega$. Variable gas properties were employed using an $8^{th}$ order piecewise polynomial for the calculation of specific heat capacity as a function of static temperature [58]. Thermal conductivity was computed according to kinetic theory as shown in Eq. (25) [54], where $M_w$ denotes the molecular weight of air. The dynamic viscosity was calculated based on Sutherland's law [59] as described in Eqs. (26), (27).

$$\lambda = \frac{15}{4}\frac{R}{M_w}\mu\left[\frac{4}{15}\frac{c_p M_w}{R} + \frac{1}{3}\right] \tag{25}$$

$$\mu = \mu_{ref}\left(\frac{\tilde{T}}{T_{ref}}\right)^{\frac{3}{2}}\frac{T_{ref}+S}{T+S} \tag{26}$$

$$\mu_{ref} = 1.716x10^{-5}\ kg/(m\cdot s), \quad T_{ref} = 273.11\ K, \quad S = 110.56\ K \tag{27}$$

## IV. Results and discussion

### A. Validation of computational approach

The numerical approach is compared against experimental data for representative conditions of nozzle over-expansion state, to assess the accuracy and soundness of the computations. In specific, the total to static pressure ratio at the inlet of the test section as well as the total pressure at the nozzle inlet is matched in the CFD within <1% of the experimental values. These conditions correspond to $NPR$=6.6 and $TPR$=1.35, as defined previously. This was the maximum NPR achieved experimentally and was sufficient to obtain representative aerodynamic conditions under over-expanded nozzle operation to validate the numerical approach. The results are shown in Figs. 6a- 6d in terms of the time-averaged

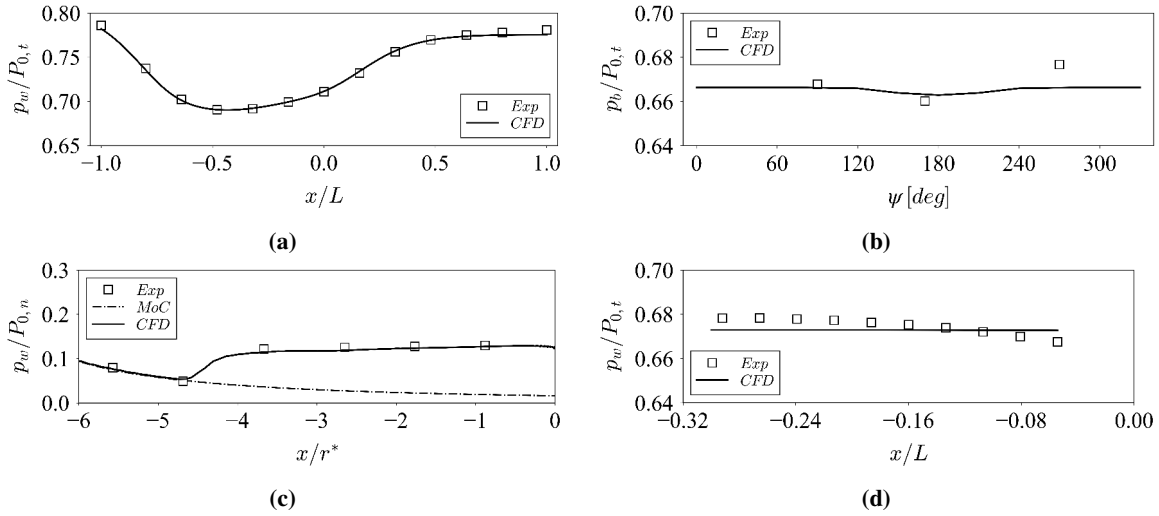


**Fig. 6 Experimental and numerical results for the pressure distribution at (a) left tunnel wall, (b) base, (c) nozzle wall and (d) cavity wall**

experimental values. Figure 6a shows the time-averaged, pressure distribution along the left wind tunnel wall (see Fig. 1). The pressure is non-dimensionalized with the total pressure at the tunnel inlet which is approximately $P_{0,t}$=101000 Pa in both experiments and CFD. The first point of the experimental results is spatially aligned with the nose of the model ($x/L$=-1), while the last one extends one model length $L$ downstream of the base. The computations properly capture the flow acceleration over the model's main body and are in good agreement with the experimental results. The azimuthal pressure distribution at the base of the model is depicted in Figure 6b. Numerical results are obtain at a constant radial location of $r/R$=0.875, with R being the model base radius, and corresponds to the radial location of the experimental transducers (Fig. 1). Again CFD is in reasonably good agreement with the experimental values, which are obtained as the temporal mean value of the signal of the Kulite sensors. Additionally, CFD properly captures the trend of the azimuthal pressure distribution at the base, exhibiting reduce levels of pressure behind the pylon ($\psi$=180°). The CFD results are symmetric with respect to $\psi$=180°, due to the half-domain approach described previously. Note that the experimental pressure measurement behind the pylon is obtained at 170° instead of 180° due practical installation reasons of this Kulite sensor.

The flow within the TIC nozzle is over-expanded, exhibiting a Free Shock Separation (FSS) state [60] with a Mach disk pattern. The numerical and experimental pressure distribution along the wall of the nozzle contour, non-dimensionalized over the total pressure at the nozzle inlet $P_{0,n}$, is depicted in Fig. 6c. The spatial location x, is non-dimensionalized with the nozzle throat radius $r^*$. Superimposed on the graph is also the ideal pressure profile calculated by the axisymmetric Method of Characteristics. Results show that computations are in very good agreement with the experimental values, and capture the incipient separation location (within the available spatial resolution in the experiments), identified as the point where the pressure profile deviates from the ideal. It is noted that this location indicates where the interaction initiates, and not the actual location where the flow separates from the nozzle wall, which corresponds to the location where the wall shear stress becomes zero. The pressure distribution in the cavity wall is also examined and presented in Fig. 6d. The computations are again in close agreement with the experimental values, although the decrease in pressure towards the base (i.e., as $x/L$ goes to 0), is somewhat steeper in the experimental values. The maximum percentage difference of the computational results with respect to the mean experimental values are reported in table 2 for the pressure distributions along the walls of the TSWT, base, cavity and nozzle. The errors are calculated as described in Eq. (28), where $\Phi$ denotes the examined variable, in this case the static to total pressure ratio.

$$\Delta\Phi(\%) = \left( \frac{|\Phi^{Exp} - \Phi^{CFD}|}{\Phi^{Exp}} \right) \cdot 100 \tag{28}$$

**Table 2 Maximum error between CFD and mean experimental values**

| Variable $\Phi$ | CFD | Exp | $\Delta\Phi_{max}$ (%) |
|---|---|---|---|
| $(p_w/P_{0,t})_{TSWT}$ | 0.7808 | 0.7754 | 0.69% |
| $(p_b/P_{0,t})_{base}$ | 0.6767 | 0.6662 | 1.55% |
| $(p_w/P_{0,t})_{cav}$ | 0.6675 | 0.6727 | 0.78% |
| $(p_w/P_{0,n})_{noz}$ | 0.1185 | 0.1200 | 1.26% |

### B. Impact of blockage on approaching flow conditions

The high blockage ratio is expected to affect the approaching flow conditions. Additionally, in the context of this work, it is important to translate the operational parameter of $TPR$, into the aerodynamic parameter of interest, which is the approach Mach number $M_a$, for each setting of the exhaust (i.e., each $NPR$). Prior knowledge of this correlation is impossible, owing to the strong influence of the blockage ratio and nozzle settings. This is depicted in Fig. 7, which

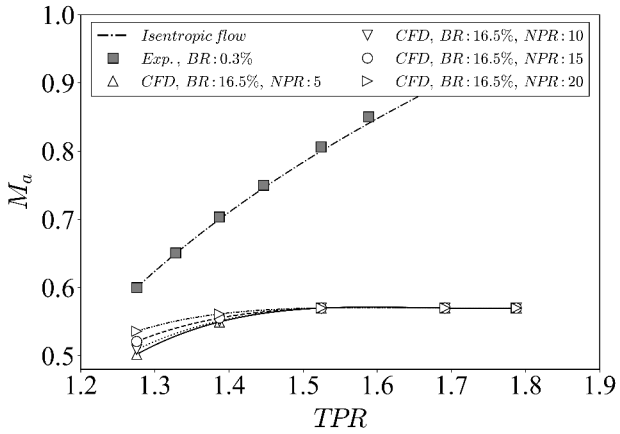


**Fig. 7 Variation of approach Mach number $M_a$ within the examined design space**

shows the variation of the approach Mach number $M_a$, measured at the tunnel inlet, as a function of the design variables, namely $TPR$ and $NPR$. The curve corresponding to fully isentropic flow is shown on the graph, along with data from a previous experimental activity in the TSWT operating nearly empty ($BR \sim 0.3\%$) [61]. A very good agreement between the experimental data and the isentropic law can be seen, indicating that under very low $BRs$, the losses within the tunnel are negligible. However, the numerical results from the tunnel-installed model, show that under the high blockage ratio of 16.5%, the approaching flow conditions are significantly different from the low $BR$ case, highlighting the influence of blockage effects. In specific, for $TPR$ above values of approximately 1.52, the flow within the wind tunnel is choked, and $M_a$ gets invariant to further increase of $TPR$ or $NPR$. The maximum approach Mach number that can be achieved within the examined design space is approximately $M_a$=0.57. At pre-choking conditions, the jet flow of the propulsive nozzle has a clear effect on the approach Mach number, which increases with increasing $NPR$ for fixed $TPRs$ as a result of the injected jet flow. This effect is more intense at low $TPRs$ and gradually diminishes as the flow

approaches the choking point.

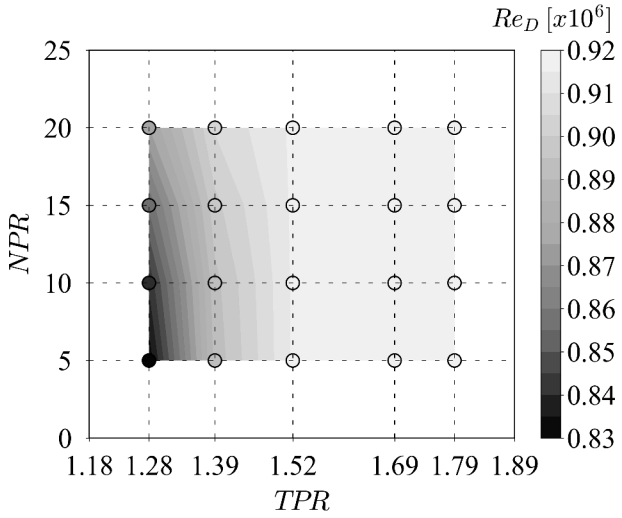


**Fig. 8 Variation of $Re_D$ in the examined design space**

Figure 8, depicts the variation of the Reynolds number at the tunnel inlet based on the model's diameter $D$, as a function of $NPR$ and $TPR$. The exact conditions of the CFD cases examined, are indicated with circles of varying color according to the corresponding value of $Re_D$. The effect of choking is visible after $TPR$ values of approximately 1.52, fixing the maximum achievable Reynolds number to values of $Re_D = 0.92 \cdot 10^6$ or accordingly $Re_L = 2.86 \cdot 10^6$ based on the maximum length of the model. Additionally, at pre-choking conditions, the behavior of Reynolds number is dominated by $TPR$ settings rather than $NPR$, which has a minor effect. Both Figs. 7 and 8 highlight the limitations in terms of maximum achievable $M_a$ and $Re_D$ within the examined conditions, as a result of increased blockage.

This analysis demonstrates that for relatively high $BRs$, it is practically unfeasible to produce free-flight equivalent conditions of transonic (and even high subsonic) flow in a closed wind tunnel configuration. In fact, based on one-dimensional isentropic flow assumption, achieving transonic approach Mach numbers of $M_a$=0.9 and 0.95, would require the blockage ratio to be drastically reduced to values of $BR$=0.88% and 0.21%, respectively [30]. Realizing that these values of $BR$ are impractical, it is essential to assess the extent of global and local flow similarity with respect to unbounded flow under large $BRs$ which are often encountered, especially in academic research facilities. It is noted that local flow similarity is somewhat irrelevant when the overall aerodynamic performance is of interest, but is critical in the context of base drag analyses.

### C. Global flow characteristics

The global flow topology of the system is described here to facilitate the qualitative characterization of the evolution of the exhaust flow across the investigated design space. Figure 9 illustrates the flow Mach number distribution in the symmetry plane $x - z$, at different conditions of $NPR$ and $TPR$. The effect of $NPR$ on the exhaust flow for fixed $TPR$

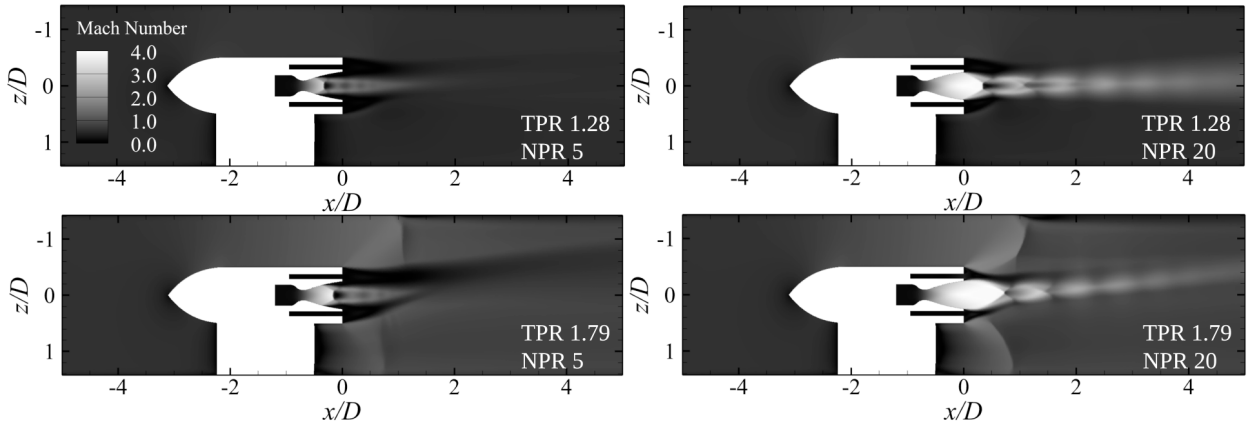


**Fig. 9 Mach number distribution for NPR=5, TPR=1.28 (top left), NPR=20, TPR=1.28 (top right), NPR=5, TPR=1.79 (bottom left) and NPR=20, TPR=1.79 (bottom right)**

of 1.28 can be seen in the top left and right figures. For $NPR$=5 the nozzle flow is highly over-expanded and at a FSS state with the Mach disk located inside the nozzle. At $NPR$=20 the flow separates just upstream of the nozzle lip, and the jet exhibits a typical shock-cell pattern. The choked flow conditions at $TPR$=1.79 are also shown for $NPR$ of 5 and 20 in the bottom left and right figures, respectively. In both cases, a clear flow expansion to supersonic speeds is visible at the vicinity of the base of the model, which coalesces into a compression shock further downstream. In the case of $NPR$=20, the expansion is intensified, resulting in a stronger compression shock, which propagates to the left tunnel wall and generates a severe, shock-induced flow separation. One can also notice the effect of increasing $TPR$ from 1.28 to 1.79 for fixed $NPR$=5, with the jet flow expanding further as a result of the lower base pressure which changes the effective $NPR$. The flow conditions under chocked tunnel operation, are strongly affected by the surrounding tunnel walls and pylon, and clearly do not represent unbounded transonic conditions, even though at the vicinity of the base, the flow can get locally transonic. Additionally, in Fig. 9 asymmetrical flow in the $x-z$ plane is visible for all cases, and manifests specifically in the flow exiting the propulsive nozzle through a jet vectoring effect. This is substantially intensified at post-choking flow conditions (bottom left and right of Fig. 9). This phenomenon was consistent in all examined cases and further analysis on its behavior and origins is performed and discussed in the following section.

*1. Jet vectoring effect*

In order to evaluate the behavior of the jet vectoring effect, a systematic metric is required. This is facilitated through the definition of the jet angle $a_j$ which is shown in Fig. 10, in this case for conditions of $NPR$=15 and $TPR$=1.69. The vorticity magnitude is also shown to visualize the exhaust flow organization. The slope of the axial streamline varies spatially and is highly dependent on the corresponding flow conditions. To overcome this ambiguity and establish consistency between the different cases, the jet angle is defined as the angle between the axis, and a line passing through two points located on the axial streamline. These are the center point of the nozzle's exit and a point located 15 diameters

$D$ downstream of the base, annotated as $P_1$ and $P_2$ in Fig. 10, respectively. In this sense, only the radial location $z/D$ of the second point $P_2(z/D, x/D = 15)$ can vary, thus providing a quantification of the axial streamline deflection with respect to the axis.

With these provisions, the jet angles for each case within the examined design space are reported in Fig. 11. The conditions corresponding to choked tunnel operation are also annotated. A systematic trend can be observed, of decreasing jet angle with increasing $NPRs$, owing to the higher flow expansion in the nozzle. Deviations from this trend are observed at conditions of $TPR$=1.52, where the jet angle is approximately the same for all $NPRs$. This is the case where choking is being established in the wind tunnel flow, and a weak normal shock is formed in the vicinity downstream of the base at a distance of around $x/D$=0.55 for all $NPRs$ (not shown here for brevity). This effectively imposes similar downstream pressure distribution to the expanding jet flow, and thus similar deflection levels. The shock strength is actually increasing with $NPR$ (similar to the cases shown in Fig. 9 for $TPR$=1.79), but at $TPR$=1.52 this increase is not sufficient to notably alter the pressure distribution downstream, and hence the jet deflection, at least not to a degree that can be captured in a time-averaged sense with RANS-based computations.

The effect of $TPR$ on the jet angle for fixed $NPRs$ is also shown in Fig. 11. At pre-choking conditions, the trend is similar for the cases of $NPR$=10, 15 and 20, with the minimum angle achieved at $TPR$=1.39. Especially in the case of $NPR$=20 and $TPR$=1.39, the jet angle is approximately zero. However, this should not be interpreted as the flow being symmetric. On the contrary, these trends demonstrate that the jet vectoring effect is dynamically affected by both wind tunnel settings and nozzle pressure ratios. For the $NPR$=5 case, an almost-linear correlation of decreasing jet angle with increasing $TPR$ can be seen up to conditions of $TPR$=1.52. This could be associated with the highly over-expanded jet flow at this $NPR$ (Fig. 9), and suggests that the base flow asymmetry is affected by a combination between the degree of expansion that is achieved in the nozzle, and the surrounding wind tunnel flow. Additionally, a discontinuous increase in the jet angle for values of $TPRs$ above 1.52 is visible in Fig. 11 for all $NPRs$, indicating that choking has a strong impact on the jet vectoring effect.

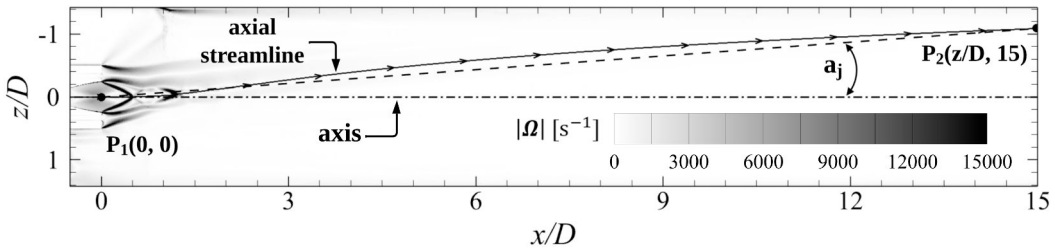


**Fig. 10 Definition of jet angle $a_j$; contours show vorticity magnitude distribution (NPR=15, TPR=1.69)**

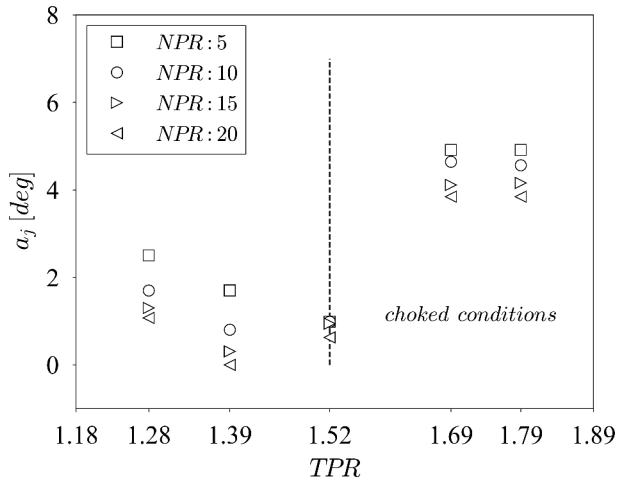


**Fig. 11 Variation of jet angle $a_j$ with TPR and NPR**

*2. Pylon impact on the jet flow*

The jet vectoring effect is further investigated in order to identify its underlying mechanism. This is facilitated through the numerical simulation of an identical exhaust system, where the effect of the tunnel walls is eliminated. In specific, a modified computational domain is constructed (not shown here for brevity), where the surfaces originally corresponding to the left and top tunnel walls (Fig. 1), are extended at a distance equal to 10 times the length of the model $L$. A pressure far-field BC is applied on these surfaces to model the free-stream conditions with the ambient static pressure and temperature, as well as the free-stream Mach number as the prescribed values. Similarly, on the surfaces originally corresponding to the tunnel inlet and outlet, the same pressure far-field BC is applied. On the surface that corresponds to the right tunnel wall (Fig. 1), a symmetry BC is applied. This approach allows for the identification

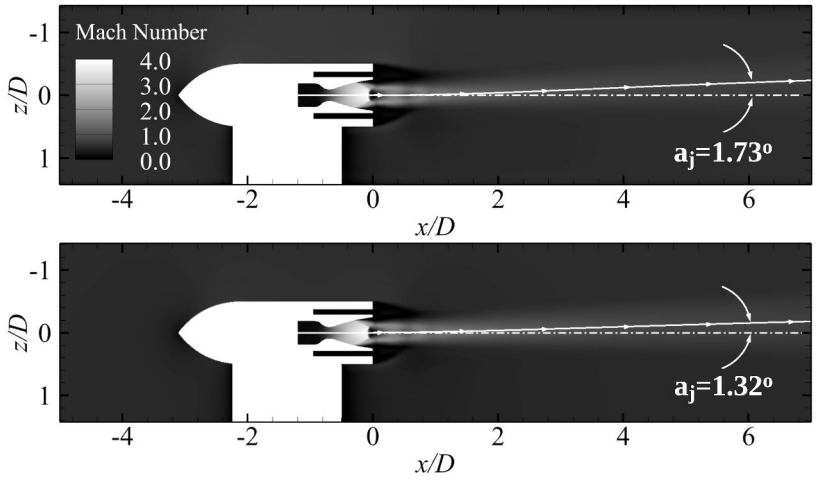


**Fig. 12 Mach number distribution for tunnel-installed (top) and unbounded (bottom) cases (NPR=10, TPR=1.28)**

of the impact of the pylon on the base flow, and eliminates any potential effect of the tunnel walls and blockage. It is noted, that for post-choking tunnel conditions, the global flow similarity with respect to unbounded flow is practically non-existent, and matching the two approaches to establish consistency in the comparison is far from trivial.

For that reason, the comparison is performed for conditions corresponding to pre-choking tunnel operation and medium $NPR$, namely $TPR$=1.28 and $NPR$=10. The free-stream Mach number for the modified domain, is matched to the approach Mach number $M_a$ for the tunnel-constrained case. The numerical approach is identical to the one described previously for the wind tunnel flow simulations. The computational mesh employs the same number of prism layers on the wall surfaces of the model (35), as well as identical spatial discretization and grid refinement regions. The remainder of the modified domain is populated with polyhedral elements of size equal to the maximum element size in the original, wind tunnel domain. It is noted that owing to the blockage effect, the flow around the model in the tunnel-constrained case cannot be exactly the same to the unbounded flow, even at low $TPRs$. However, the objective of this analysis is to investigate the impact of the pylon on the exhaust flow asymmetry at the absence of the tunnel walls. Figure 12 depicts the Mach number distribution for the tunnel-installed case (top) and the free-stream, unbounded flow case (bottom). As shown, the jet vectoring effect still manifests in the absence of the walls of the wind tunnel, confirming that the origin is the asymmetry caused by the existence of the pylon. The jet angle $a_j$, is also annotated in the figure for both cases, and is approximately 30% higher in the tunnel-constrained flow. Additionally, the achieved flow expansion at the nacelle afterbody is slightly higher in the tunnel-installed case as a result of the blockage.

The employed computational mesh (Fig. 5), is not symmetric as a result of the pylon wake flow that needs to be sufficiently captured. In specific, the computational grid features increased spatial resolution downstream of the pylon compared to the region between the main cylindrical body and the left tunnel wall ($z/D$ <0). The potential impact of the discretization asymmetry on the jet vectoring phenomenon is also investigated. The pylon is removed from the wind

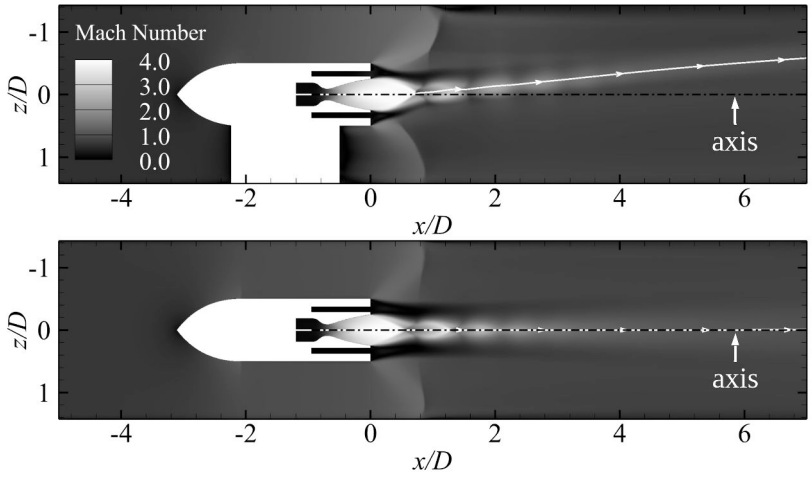


**Fig. 13 Mach number distribution for the installed (top) and axisymmetric (bottom) cases (NPR=20, TPR=1.79)**

tunnel computational domain, making the configuration axially symmetric, while maintaining identical, non-symmetric meshing approach as the one for the installed model. The computational mesh for this case is slightly smaller as a result of the absence of the pylon. The numerical strategy is kept identical.

Figure 13 shows the Mach number distribution at conditions of $TPR_{max}$=1.79 and $NPR_{max}$=20 for the installed case (top) and the case corresponding to axially symmetric configuration (bottom). It is shown that the configuration without the pylon, features a fully-symmetric flow topology even at post-choking tunnel conditions, and the propulsive jet is not vectored, regardless of the existing asymmetry in the computational grid. Furthermore, it is demonstrated that tunnel choking has no effect on the symmetry of the surrounding flow at the absence of the pylon. However, once flow asymmetry is established through the pylon, tunnel choking seems to intensify its impact on the exhaust flow (Fig. 11). The asymmetry that is caused by the pylon, which has a symmetric airfoil profile cross-section, is linked with the associated flow separation. While this canonical geometry is not representative of actual high-speed exhausts of future propulsion systems (no swept-wing configuration, large thickness, etc.), the results indicate that the wing can affect the jet flow, especially at over-expanded conditions. Several high-speed vehicle concepts feature tip-mounted engines [62–64], and therefore the extent of this impact should be investigated in future studies, focusing into airframe-engine installation effects on the exhaust flow and performance.

### D. Local flow characteristics

The preceding analysis focused on the effects of wind tunnel installation on the global flow characteristics of the investigated apparatus. Even though there is indeed a region of the design space corresponding to pre-choking operation where experimental measurements could potentially be corrected to represent unbounded-equivalent flow conditions, the application of such corrections for a complex configuration, which is strongly influenced by blockage effects, as well as nozzle and tunnel settings, is far from trivial. Additionally, as discussed previously, such installation effects due to high blockage can be quite common in academic facilities, owing to the combination of small wind tunnels [28] and the requirement for a relatively large model. However, in the context of base flows, it is usually the local flow characteristics at the surface of the base that are of specific interest [14, 22, 26]. Consequently, it is important and of practical value, to investigate whether a tunnel-constrained flow could feature local flow similarity at the base with respect to unbounded flow conditions, even if the global flow topology differs notably. In this study, a systematic approach to address this question is employed and presented in this section.

#### *1. Rationale*

Base flow similarity is examined between the model installed in the tunnel, and an identical, axially symmetric geometry, corresponding to unbounded flow conditions. Installation effects caused by the pylon, tunnel walls and blockage are totally removed from the unbounded case. Therefore, a two-dimensional and axisymmetric computational

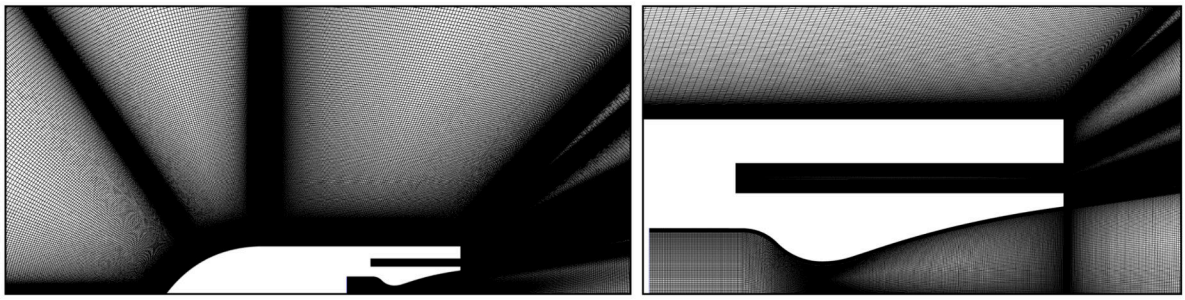

**Fig. 14 Mesh employed for unconstrained flow conditions (left) and colse-up view on base region (right)**

approach is employed, using an implicit, density-based and compressible, RANS solver [54]. The numerical approach adopted for this analysis is identical to the one described previously for the three-dimensional, tunnel-installed model. The domain is discretized using a multi-block, fully structured grid approach [65]. The computational domain, boundary conditions as well as meshing approach, are adopted from previous work [26], involving an identical configuration under unbounded conditions, featuring a slightly modified cavity shape. Figure 14 shows the computational mesh employed for this study (left) along with a close-up view on the cavity and nozzle regions (right). The GCIs [53] corresponding to the medium mesh for the drag and nozzle standard velocity coefficients ($C_d$ and $C_{V,s}$), are 0.26% and 0.75%, respectively. Consequently, the medium grid size of approximately 1.2 million cells is employed for the analysis [26].

Wind tunnel installation effects and high blockage in specific, notably affect the flow surrounding the model in the tunnel, even at pre-choking conditions [30] as shown previously (Fig. 7). This makes the comparison between the two cases in terms of flow conditions, anything but straightforward. In other words, there is no way to know a priori what are the conditions that need to be prescribed in the unbounded case (i.e., $M_\infty$), to match the conditions in the vicinity of the base of the model in the tunnel. In this study, we propose a methodology to allow for proper comparison of the base flows between the tunnel-constrained and equivalent unbounded flow cases. The approach is based on systematic comparison of the static pressure distribution at the base surface, which is critical in experimental base flows and base drag analysis in specific [22, 25]. The employed metric of interest, on the basis of which the analysis is established, is the effective Mach number at the end of the afterbody expansion, immediately upstream of the base surface, denoted as $M_{aft}^{eff}$ and defined in Eq. (29) as a function of the azimuthal angle $\psi$.

$$M_{aft}^{eff}(\psi) = \left[ \frac{2}{(\gamma - 1)} \left( \left( \frac{P_0}{p_{aft}^{\psi}} \right)^{\frac{\gamma-1}{\gamma}} - 1 \right) \right]^{\frac{1}{2}} \tag{29}$$

This is the Mach number that would be achieved theoretically, under isentropic flow assumption, depending on the pressure ratio between the total pressure $P_0$, and the local static pressure $p_{aft}^{\psi}$ on the nacelle shoulder, immediately upstream of the base surface. The superscript $\psi$ indicates the corresponding azimuthal angle in the $y - z$ plane (Fig. 1),

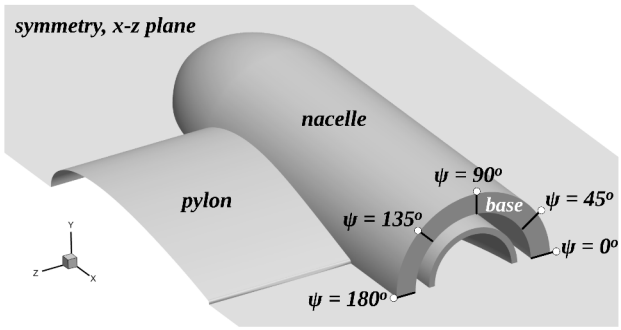


**Fig. 15 Azimuthal angles $\psi$ along the base surface**

where the pressure value is extracted ($0< \psi <180$) for the tunnel-installed case. The total pressure $P_0$ in Eq. (29) is atmospheric for both unbounded and tunnel-constrained cases. Consequently, $M_{aft}^{eff}$ represents directly the local static pressure at the end of the afterbody flow expansion, and allows to map the design variables for each case at a given $NPR$, through the functions $M_{aft}^{eff}=f(TPR)$ and $M_{aft}^{eff}=f(M_\infty)$, respectively. Therefore, this approach allows for a comparison to be made on the basis of a local flow similarity parameter, and hence, to quantify to what extent the base pressure distribution is similar. This methodology could be applied to any base flow analysis of blunt-based bodies, for both power-off and power-on configurations.

*2. Base flow mapping*

The analysis initially requires knowledge of the achieved flow expansion at the model shoulder in the unbounded case, that is, construction of the mapping function $M_{aft}^{eff}=f(M_\infty)$ for a given $NPR$. For this analysis, a medium $NPR$ of 10 is selected for both tunnel-constrained and unbounded cases, as it includes both high and low degrees of over-expansion within the range of $1.28< TPR <1.79$. A sweep of $M_\infty$ values is performed for the unbounded flow, in the range of $0.5< M_\infty <1.5$ with a step of 0.05, producing a total number of 21 simulations. The effective Mach number is extracted for each $M_\infty$ case as the average value across a length corresponding to approximately three computational cells upstream of the base. This is done to avoid numerical instability and discontinuity at the singularity formed between the nacelle shoulder and base surfaces. The same procedure is applied for the tunnel-installed cases corresponding to a sweep of $TPRs$ in the range $1.28< TPR <1.79$ and $NPR$=10, to retrieve the mapping function $M_{aft}^{eff}=f(TPR)$. In this case, $M_{aft}^{eff}$ is an average of the effective Mach numbers, extracted at five different azimuthal locations as shown in Fig. 15 ($\psi$=0°, 45°, 90°, 135°and 180°) to take into account three-dimensionality effects caused by the blockage, tunnel walls and pylon.

Figure 16 depicts the mapping of free-stream Mach numbers $M_\infty$, to tunnel pressure ratio settings, on the basis of the effective Mach number at the end of the afterbody, for $NPR$=10. For the unbounded case, the trend of the flow expansion at the nacelle and afterbody, is modified above supersonic $M_\infty$ values. Therefore, it is split between the regions corresponding to subsonic and supersonic flow conditions (i.e., $0.5\leq M_\infty<1$ and $1\leq M_\infty\leq 1.5$). Through the

mapping shown in Fig. 16, it is now possible to retrieve the free-stream conditions that would produce the same $M_{aft}^{eff}$ at any given setting of $TPR$. This is required in order to establish proper base flow similarity comparison between the tunnel-constrained and unbounded flows, owing to the large blockage ratio.

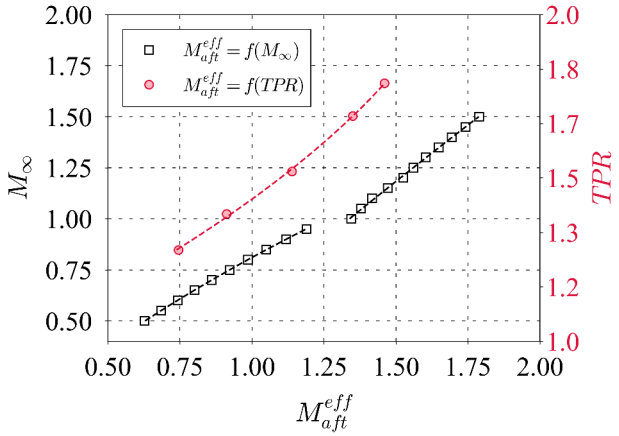


**Fig. 16 Mapping of $M_\infty$-TPR through $M_{aft}^{eff}$ for unbounded and tunnel-constrained flows (NPR=10)**

*3. Base flow similarity comparison*

Based on the methodology described above, the free-stream Mach number of the unbounded flow, is adjusted to match the azimuthal average $M_{aft}^{eff}$ of the tunnel-constrained case (within <0.6%) for each examined $TPR$ at $NPR$=10. The pressure distribution at the base and cavity surfaces is then compared between the unbounded and tunnel-constrained flows to assess the local flow similarity characteristics. The radial location $r$ where the surface pressure data is taken, non-dimensionalized over the model's radius $R$, is shown in Fig. 17 ($0.575 \leq r/R \leq 0.75$ for the cavity wall and $0.75 \leq r/R \leq 1$ for the base). Figures 18a through 18e show the variation of $(p_b^\psi / P_0)$ along the surfaces of the cavity side wall and base for each corresponding $TPR$ value. For the wind tunnel case, the base pressure distribution at all five azimuthal angles is included ($\psi$=0°, 45°, 90°, 135°and 180°), to assess three-dimensionality effects.

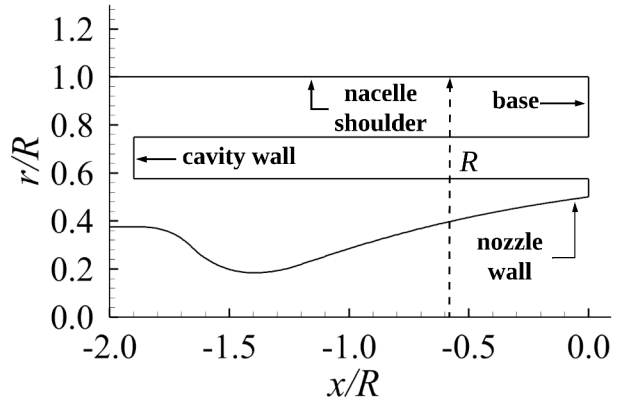


**Fig. 17 Schematic of base geometry**

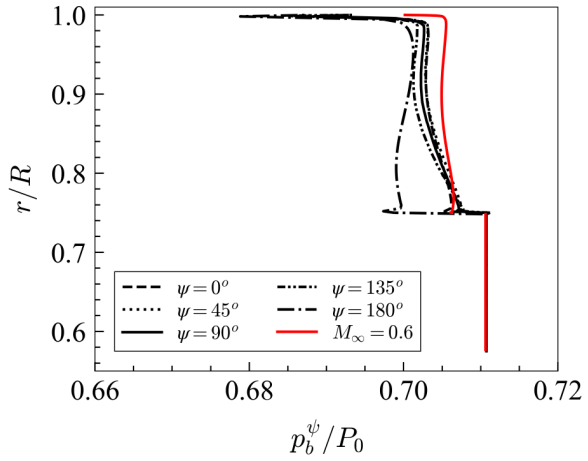


**(a) TPR=1.28, average $M_{aft}^{eff}$=0.743**

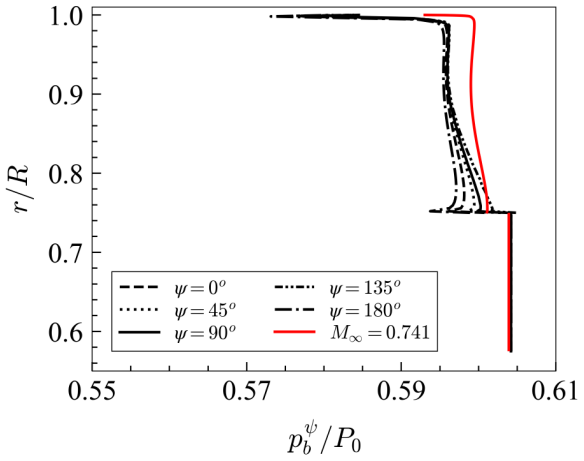


**(b) TPR=1.39, average $M_{aft}^{eff}$=0.911**

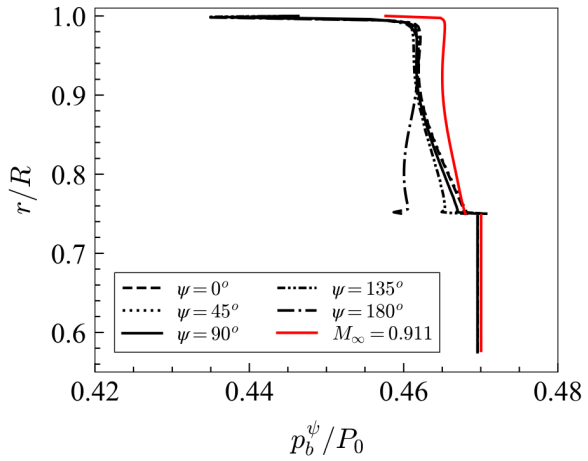


**(c) TPR=1.52, average $M_{aft}^{eff}$=1.138**

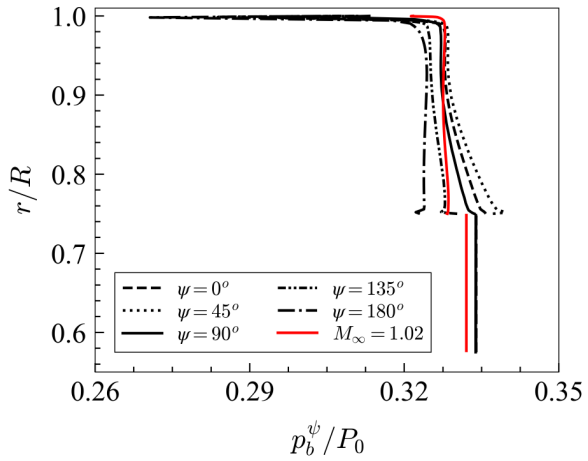


**(d) TPR=1.69, average $M_{aft}^{eff}$=1.355**

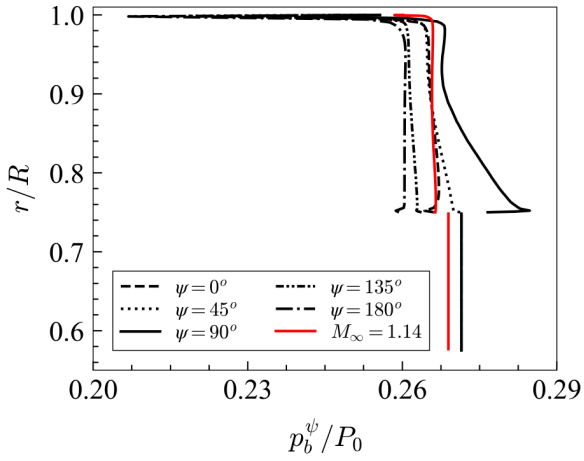


**(e) TPR=1.79, average $M_{aft}^{eff}$=1.460**

**Fig. 18 Base and cavity pressure distribution for tunnel-constrained and unbounded cases at NPR=10**

In Fig. 18, it can be seen that the base pressure distribution of the unbounded case agrees reasonably good against the tunnel-constrained flow for all $TPRs$ (pre- and post-choking), while the pressure along the cavity wall is in very good agreement, indicating that the proposed methodology is sound and can be employed. The two flow topologies exhibit some differences in the behavior of the flow expansion at the base edge, as expected due to the constriction of the flow. In specific, the flow in the tunnel-constrained case, expands further to lower pressures for a short region along the base surface, in the range of $0.995< r/R <1$, before pressure recovery initiates, in contrast to the unbounded flow where pressure recovery initiates almost immediately at the base edge. Note that, even though the average effective Mach number just upstream of the base is matched within less than 0.6% between the two flows, an exact match is not possible, owing to the blockage and three-dimensionality effects caused by the pylon, leading to an azimuthal variation of the static pressure in the wind tunnel flow. This short expansion region in the wind tunnel case (i.e., $0.995< r/R <1$) corresponds to less than 1.5% of the total examined base surface area, including the cavity wall. Additionally, its actual length in this case, is smaller than the size of most miniaturized dynamic pressure transducers, making it trivial in the context of experimental measurements for base flows in academic research facilities. Neglecting this region, the maximum deviation at pre-choking conditions in the range of $0.575< r/R <0.995$ (i.e., above 98.5% of the base surface area) and $0^o \leq \psi \leq 135^o$ , is less than 0.7%. As expected, this value can increase by a factor of 2 for the region behind the pylon, which exhibits reduced pressure levels as indicated with the lines corresponding to azimuthal angle $\psi$=$180^o$, and is not present in the examined unbounded flow scenario. This demonstrates the non-negligible interference effects caused by the presence of the pylon. The pressure distribution along the cavity side wall agrees within less than 0.1%.

For the cases corresponding to post-choking conditions of $TPR$=1.69 and 1.79, a higher variation can be seen in the base pressure of the tunnel-constrained case, depending on the azimuthal location. This variation can reach values of approximately 7.5% at $TPR$=1.79 between angles of $90^o$ and $180^o$. This is not unexpected, since these are the locations where the wind tunnel wall has the smallest distance from the model ($\psi$=$90^o$) and behind the pylon ($\psi$=$180^o$), respectively. The pressure at the cavity wall recovers to the same values, regardless of the azimuthal angle for both $TPRs$ of 1.69 and 1.79. The base pressure distribution of the unbounded flow falls within the observed azimuthal pressure range of the tunnel-constrained flow as shown in Figs. 18d and 18e. The maximum deviation in base pressure between the unbounded and tunnel-constrained flow conditions for the $TPRs$=1.69 and 1.79 cases, is approximately 3.2% and 6%, respectively, identified closer to the cavity ($\sim r/R$=0.75). Note that the azimuthal variation of pressure recovery for $TPRs$ 1.69 and 1.79 is a result of the location and strength of the formed shock waves after the flow expansion (Fig. 9), as well as the state of the nozzle flow. The pressure distribution along the cavity wall agrees within less than 0.57% and 1% with respect to the tunnel-constrained flow, for $TPRs$ of 1.69 and 1.79, respectively. Consequently, reasonably good local base flow similarity, in terms of pressure distribution, can be established between tunnel-constrained and unbounded flow conditions, on the basis of $M_{aft}^{eff}$.

# V. Conclusions

Experimental studies are necessary for the development of future, high-speed propulsion systems that could enable faster transportation and routine space-access. However, experimental testing has limitations, including blockage as well as tunnel-walls and support interference effects. In this study, the wind tunnel installation effects on the exhaust flow of a high-speed system under a large blockage ratio of 16.5% are examined numerically. The configuration features a cold flow, TIC nozzle along with an axisymmetric cavity region at the base, and is representative of future, advanced propulsion concepts, usually incorporating base-embedded nozzles and cavities. The work is motivated by the size of most closed transonic tunnels currently available in academic research facilities and the need for testing relatively large, powered-on models, both leading to high blockage ratios, and hence severe distortion of the flow. Additionally, in the context of base flows, it is the local pressure characteristics at the base that are typically of primary interest. Therefore, the objective of the work is partially to address whether local base flow similarity exists with respect to unbounded flow conditions.

Three-dimensional, Favre-averaged Navier-Stokes computations are used for the analysis. The employed numerical approach is validated against experimental data from a dedicated tunnel campaign at representative conditions corresponding to over-expanded nozzle state. Several wind tunnel and nozzle settings are examined in terms of $TPR$ and $NPR$. Due to the large blockage ratio, the approach Mach number is limited to values of 0.57 before choking occurs in the tunnel. At pre-choking conditions, increase in the $NPR$, leads to higher approach Mach numbers as a result of the added jet flow. Furthermore, severe distortion of the exhaust flow is observed, and a systematic vectoring effect of the jet is identified which is enhanced under choked tunnel conditions. Its origin is found to be solely due to the existence of the pylon. This provides important insight into the aerodynamic characteristics of installed high-speed exhaust flows as it could lead to undesirable base flow asymmetry in future tip-mounted systems, such as those typically employed in high-speed vehicle concepts [62].

Additionally, local base flow similarity with respect to unbounded flow conditions is examined in terms of base pressure distribution. To achieve this, a novel approach is derived and proposed which can establish comparability between the two cases and is based on the effective Mach number at the end of the afterbody expansion, $M_{aft}^{eff}$. Results indicate good comparison of base pressure distribution between the tunnel-constrained and unbounded flow conditions. In specific, for pre-choking conditions, base pressure agrees within less than 0.7%. This value can increase by a factor of 2 downstream of the pylon, which is not present in the unbounded flow conditions. The pressure distribution along the cavity wall is in excellent agreement between the two cases and below 0.1%. At post-choking conditions, the exhaust flow in the tunnel is severely distorted and the pressure distribution at the base exhibits increased variations of up to 7.5% depending on the azimuthal location. Still, the pressure distribution of the unbounded case compares reasonably well and falls within the observed range, while the comparison along the cavity wall is below 1%.

The results demonstrate that the proposed approach can establish local aerodynamic similarity at the base between

tunnel-constrained and in-flight high-speed exhaust systems, even if the global flow features are different due to large blockage. This enables small-scale testing facilities to be used for base flow analyses under high blockage ratios. Additionally, this approach has broader application to blunt-based geometries and is pertinent to base flow studies of space launch systems.

## Acknowledgments

The authors would like to express their gratitude to Reaction Engines Ltd., Rolls-Royce Plc., and the Cranfield Air and Space Propulsion Institute (CASPI) for funding this project and granting permission to publish this research. The support of Dr Mark Finnis in the experimental set-up is greatly acknowledged.

## References

[1] Varvill, R., and Bond, A., "A comparison of propulsion concepts for SSTO reusable launchers," *Journal of the British Interplanetary Society*, Vol. 56, 2003, pp. 108–117.

[2] McClinton, C. R., "High speed/hypersonic aircraft propulsion technology development," *Advances on propulsion technology for high-speed aircraft. Educational Notes RTO-EN-AVT-150*, Vol. 1, NATO RTO, Neuilly-sur-Seine, France, 2007, pp. 1–32.

[3] Ingenito, A., *Subsonic Combustion Ramjet Design*, Springer Nature, Switcherland, 2021. https://doi.org//10.1007/978-3-030-66881-5, chapter 3.

[4] Murthy, S., and Curran, E., *Scramjet Propulsion*, AIAA, 2001. https://doi.org/10.2514/4.866609, chapter 6.

[5] Bogar, T., Eiswirth, E., Couch, L., Hunt, J., and McClinton, C., "Conceptual design of a Mach 10, global reach reconnaissance aircraft," *32nd Joint Propulsion Conference and Exhibition*, 1996. https://doi.org/10.2514/6.1996-2894.

[6] Daines, R., and Segal, C., "Combined Rocket and Airbreathing Propulsion Systems for Space-Launch Applications," *Journal of Propulsion and Power*, Vol. 14, No. 5, 2012, pp. 605–612. https://doi.org/10.2514/2.5352.

[7] Jian, D., and Qiuru, Z., "Key technologies for thermodynamic cycle of precooled engines: A review," *Acta Astronautica*, Vol. 177, 2020, pp. 299–312. https://doi.org/10.1016/j.actaastro.2020.07.039.

[8] Tsentis, S., Gkoutzamanis, V., Gaitanis, A., and Kalfas, I., "Multi-platform App-embedded Model for Hybrid Air-Breathing Rocket-Cycle Engine in Hypersonic Atmospheric Ascent," *The Aeronautical Journal*, Vol. 125 (1291), 2021, pp. 1631–1653. https://doi.org/10.1017/aer.2021.3.

[9] Villace, V. F., and Paniagua, G., "Simulation of a Combined Cycle for High Speed Propulsion," *48th AIAA Aerospace Sciences Meeting Including the New Horizons Forum and Aerospace Exposition*, Orlando, Florida, 2010. https://doi.org/10.2514/6.2010-1125.

[10] Mariotti, A., and Buresti, G., "Experimental investigation on the influence of boundary layer thickness on the base pressure and near-wake flow features of an axisymmetric blunt-based body," *Experiments in Fluids*, Vol. 54, No. 1612, 2013. https://doi.org/10.1007/s00348-013-1612-5.

[11] Mariotti, A., Buresti, G., and Salvetti, M. V., "Connection between base drag, separating boundary layer characteristics and wake mean recirculation length of an axisymmetric blunt-based body," *Journal of Fluids and Structures*, Vol. 55, 2015, pp. 191–203. https://doi.org/10.1016/j.jfluidstructs.2015.02.012.

[12] Tran, T., Dinh, H., and Chu, H. e. a., "Effect of boattail angle on near-wake flow and drag of axisymmetric models: a numerical approach," *Journal of Mechanical Science and Technology*, Vol. 35, 2021, pp. 563–573. https://doi.org/10.1007/s12206-021-0115-1.

[13] Deprés, D., Reijasse, P., and Dussauge, J. P., "Analysis of Unsteadiness in Afterbody Transonic Flows," *AIAA Journal*, Vol. 42, No. 12, 2004, pp. 2541–2550. https://doi.org/10.2514/1.7000.

[14] Paciorri, R., Sabetta, F., Valenza, F., Fauci, R., Passaro, A., and Baccarella, D., "Base-Pressure Experimental Investigation on a Space Launcher in Subsonic Regime," *Journal of Spacecraft and Rockets*, Vol. 50, No. 3, 2013, pp. 572–578. https://doi.org/10.2514/1.A32283.

[15] Statnikov, V., Sayadi, T., Meinke, M., Schmid, P., and Schröder, W., "Analysis of pressure perturbation sources on a generic space launcher after-body in supersonic flow using zonal turbulence modeling and dynamic mode decomposition," *Physics of Fluids*, Vol. 27, No. 016103, 2015. https://doi.org/10.1063/1.4906219.

[16] Saile, D., Kühl, V., and Gülhan, A., "On the subsonic near-wake of a space launcher configuration with exhaust jet," *Experiments in Fluids*, Vol. 60, No. 165, 2019. https://doi.org/10.1007/s00348-019-2801-7.

[17] Schwane, R., "Numerical Prediction and Experimental Validation of Unsteady Loads on ARIANE5 and VEGA," *Journal of Spacecraft and Rockets*, Vol. 52, No. 1, 2015, pp. 54–62. https://doi.org/10.2514/1.A32793.

[18] Saile, D., Kühl, V., and Gülhan, A., "On subsonic near-wake flows of a space launcher configuration with various base geometries," *Experiments in Fluids*, Vol. 62, No. 122, 2021. https://doi.org/10.1007/s00348-021-03149-z.

[19] Hammond, W. E., *Design Methodologies for Space Transportation Systems*, AIAA, Virginia, 2001. https://doi.org/10.2514/4.861734.

[20] Meliga, P., and Reijasse, P., "Unsteady Transonic Flow Behind An Axisymmetric Afterbody Equipped With Two Boosters," *25th AIAA Applied Aerodynamics Conference*, 2012. https://doi.org/10.2514/6.2007-4564.

[21] Morel, T., "Effect of Base Cavities on the Aerodynamic Drag of an Axisymmetric Cylinder," *Aeronautical Quarterly*, Vol. 30, 1990, pp. 400–412. https://doi.org/10.1017/s0001925900008611.

[22] Tripathi, A., Manisankar, C., and Verma, S. B., "Control of base pressure for a boat-tailed axisymmetric afterbody via base geometry modifications," *Aerospace Science and Technology*, Vol. 45, 2015, pp. 284–293. https://doi.org/10.1016/j.ast.2015.05.021.

[23] Viswanath, P. R., and Patil, S. R., "Effectiveness of passive devices for axisymmetric base drag reduction at Mach 2," *Journal of Spacecraft and Rockets*, Vol. 27, No. 3, 1990, pp. 234–237. https://doi.org/10.2514/3.26130.

[24] Viswanath, P. R., "Flow Management Techniques for Base and Afterbody Drag Reduction," *Progress in Aerospace Sciences*, Vol. 32, 1996, pp. 79–129. https://doi.org/10.1016/0376-0421(95)00003-8.

[25] Tanner, M., "Reduction of Base Drag," *Progress in Aerospace Sciences*, Vol. 16, No. 4, 1975, pp. 369–384. https://doi.org/10.1016/0376-0421(75)90003-2.

[26] Tsentis, S., Goulos, I., Prince, S., Pachidis, V., and Zmijanovic, V., "Propulsion Aerodynamics for a Novel High-Speed Exhaust System," *Journal of Engineering for Gas Turbines and Power*, 2023, pp. 1–33. https://doi.org/10.1115/1.4063416.

[27] Roncioni, P., Vitagliano, P., Gregorio, F., Pezzella, G., Romano, L., and Paglia, F., "Aerodynamic Appraisal of the VEGA-C Launcher," *Journal of Spacecraft and Rockets*, Vol. 60, No. 5, 2023, pp. 1422–1436. https://doi.org/10.2514/1.A35610.

[28] Greenwell, D., "Transonic industrial wind tunnel testing in the 2020s," *The Aeronautical Journal*, Vol. 126, No. 1295, 2022, p. 125–151. https://doi.org/10.1017/aer.2021.107.

[29] Chanetz, B., Délery, J., Gilliéron, P., Gnemmi, P., Gowree, E. R., and Perrier, P., *Experimental Aerodynamics: An Introductory Guide*, Springer Cham, 2020. https://doi.org/https://doi.org/10.1007/978-3-030-35562-3.

[30] Goethert, B. H., "Transonic Wind Tunnel Testing," AGARDograph No. 49, Advisory Group for Aerospace Research and Development, 7 Rue Ancelle 92200 Neuilly, Sur Seine, France, 1961.

[31] Marschner, B., "The Flow Over a Body in a Choked Wind Tunnel and in a Sonic Free Jet," *Journal of the Aeronautical Sciences*, Vol. 23, No. 4, 1956, pp. 368–376. https://doi.org/10.2514/8.3567.

[32] Engineering Sciences Data Unit (ESDU), "Blockage corrections for bluff bodies in confined flows," Tech. Rep. ESDU 80024, London, UK, Nov. 1980. With Amendments A, March 1998.

[33] Saathoff, P., and Melbourne, W., "Freestream turbulence and wind tunnel blockage effects on streamwise surface pressures," *Journal of Wind Engineering and Industrial Aerodynamics*, Vol. 26, No. 3, 1987, pp. 353–370. https://doi.org/10.1016/0167-6105(87)90005-5.

[34] Choi, C.-K., and Kwon, D.-K., "Wind tunnel blockage effects on aerodynamic behavior of bluff body," *Wind and Structures*, Vol. 1, No. 4, 1998, pp. 351–364. https://doi.org/10.12989/was.1998.1.4.351.

[35] Huang, J., Gu, M., and Gao, Y., "Blockage effects on aerodynamics of isolated tall buildings under uniform turbulent flows," *Journal of Wind Engineering and Industrial Aerodynamics*, Vol. 212, 2021, p. 104607. https://doi.org/10.1016/j.jweia.2021.104607.

[36] Katz, J., *Race Car Aerodynamics*, 2nd ed., Robert Bentley, Cambridge, MA, 2006. Chapter 3, pp. 69–71.

[37] van Gent, P. L., Payanda, Q., Brust, S. G., van Oudheusden, B. W., and Schrijer, F. F. J., "Effects of Exhaust Plume and Nozzle Length on Compressible Base Flows," *AIAA Journal*, Vol. 57, No. 3, 2019, pp. 1184–1199. https://doi.org/https://doi.org/10.2514/1.J057314.

[38] Schreyer, A.-M., Stephan, S., and Radespiel, R., "Characterization of the supersonic wake of a generic space launcher," *CEAS Space Journal*, Vol. 9, 2017, pp. 97–110. https://doi.org/10.1007/s12567-016-0134-4.

[39] Schreyer, A.-M., "Flow structure in the wake of a space-launcher model with propulsive-jet simulation," *CEAS Space Journal*, Vol. 12, 2020, pp. 367–383. https://doi.org/10.1007/s12567-020-00306-8.

[40] MIDAP, S. G., "Subsonic Wind Tunnel Wall Corrections," AGARDograph No. 109, Advisory Group for Aerospace Research and Development, 7 Rue Ancelle 92200 Neuilly, Sur Seine, France, 1966.

[41] MIDAP, S. G., "Wind Tunnel Wall Correction," AGARDograph No. 336, Advisory Group for Aerospace Research and Development, 7 Rue Ancelle 92200 Neuilly, Sur Seine, France, 1998.

[42] Saddington, A., Knowles, K., and Thangamani, V., "Scale effects on the performance of sawtooth spoilers in transonic rectangular cavity flow," *Experiments in Fluids*, Vol. 57, No. 2, 2016. https://doi.org/10.1007/s00348-015-2088-2.

[43] Zucrow, M. J., and Hoffman, J. D., *Gas Dynamics*, John Wiley and Sons, New York, 1976.

[44] Sauer, R., "General Characteristics of the Flow through Nozzles at Near Critical Speeds," Memorandum No.1147, NACA, Washington, DC, 1947.

[45] MIDAP, S. G., "Guide to In-Flight Thrust Measurement of Turbojets and Fan Engines," AGARDograph No. 237, Advisory Group for Aerospace Research and Development, 7 Rue Ancelle 92200 Neuilly, Sur Seine, France, 1979.

[46] Wilcox, D., *Turbulence Modeling for CFD*, DCW Industries, La Canada, California, 2006.

[47] Menter, F. R., "Two-equation eddy-viscosity turbulence models for engineering applications," *AIAA Journal*, Vol. 32, No. 8, 1994, pp. 1598–1605. https://doi.org/10.2514/3.12149.

[48] Menter, F., Kuntz, M., and Langtry, R., "Ten Years of Industrial Experience with the SST Turbulence Model," *Heat and Mass Transfer 4*, Begell House Inc., 2003, pp. 625–632.

[49] *Ansys FLUENT Meshing User Guide*, Ansys Inc., 275 Technology Drive, Canonsburg, PA 15317, 2012.

[50] Zhou, C., and Chen, M., "Aerodynamic Simulation of Helicopter Based on Polyhedron Nested Grid Technology," *Applied Sciences*, Vol. 10, No. 22:8304, 2020. https://doi.org/10.3390/app10228304.

[51] Wang, W., Cao, Y., and Okaze, T., "Comparison of hexahedral, tetrahedral and polyhedral cells for reproducing the wind field around an isolated building by LES," *Building and Environment*, Vol. 195, No. 107717, 2021. https://doi.org/10.1016/j.buildenv.2021.107717.

[52] Richardson, L. F., and Gaunt, J. A., "The Deferred Approach to the Limit," *Philos. Trans. R. Soc. London*, Vol. Ser. A, 226, 1927, pp. 307–357.

[53] Celik, I. B., Ghia, U., Roache, P. J., Freitas, C. J., Coleman, H., and Raad, P. E., "Procedure for Estimation and Reporting of Uncertainty Due to Discretization in CFD Applications," *Journal of Fluids Engineering*, Vol. 130, No. 7, 2008. https://doi.org/10.1115/1.2960953.

[54] *Ansys Fluent Theory Guide*, Ansys Inc., 275 Technology Drive, Canonsburg, PA 15317, 2013.

[55] Allamaprabhu, C., Raghunandan, B., and Morinigo, J., "Improved Prediction of Flow Separation in Thrust Optimized Parabolic Nozzles with FLUENT," *47th AIAA/ASME/SAE/ASEE Joint Propulsion Conference & Exhibit*, San Diego, California, 2011. https://doi.org/10.2514/6.2011-5689.

[56] Hasan, R. G. M., McGuirk, J. J., Apsley, D. D., and Leschziner, M. A., "A turbulence model study of separated 3D jet/afterbody flow," *The Aeronautical Journal*, Vol. 108, No. 1079, 2004, p. 1–14. https://doi.org/10.1017/S0001924000004942.

[57] Roe, P. L., "Approximate Riemann solvers, parameter vectors, and difference schemes," *Journal of Computational Physics*, Vol. 43, No. 2, 1981, pp. 357–372. https://doi.org/10.1016/0021-9991(81)90128-5.

[58] *Ansys Fluent User's Guide*, Ansys Inc., 275 Technology Drive, Canonsburg, PA 15317, 2021.

[59] Sutherland, W., "The viscosity of gases and molecular forces," *Philos. Mag.*, Vol. 36, 1893, pp. 507–531.

[60] Nasuti, F., and Onofri, M., "Shock structure in separated nozzle flows," *Shock Waves*, Vol. 19, 2009, pp. 229–237. https://doi.org/10.1007/s00193-008-0173-7.

[61] Debiasi, M. T., Atkinson, K., Saddington, A., and Finnis, M., "Aero-whisker for the Measurement of Aircraft Flight Speed and Angle of Attack in Compressible Flow Conditions," *AIAA AVIATION 2023 Forum*, San Diego, CA, 2023. https://doi.org/10.2514/6.2023-4079.

[62] Mehta, U., Aftosmis, M., Bowles, J., and Pandya, S., "Skylon Aerospace Plane and Its Aerodynamics and Plumes," *Journal of Spacecraft and Rockets*, Vol. 53, No. 2, 2016, pp. 340–353. https://doi.org/10.2514/1.A33408.

[63] Brevault, L., Balesdent, M., Wuilbercq, R., Subra, N., Oriol, S., Bonnal, C., Dodds, M., Taylor, N. V., and Varvill, R., "Conceptual design of a Two-Stage-To-Orbit vehicle using SABRE engines," 2019. https://doi.org/10.13009/EUCASS2019-454.

[64] Steelant, J., Varvill, R., Walton, C., Defoort, S., Hannemann, K., and Marini, M., "Achievements Obtained for Sustained Hypersonic Flight within the LAPCAT-II project," *20th AIAA International Space Planes and Hypersonic Systems and Technologies Conference*, 2015. https://doi.org/10.2514/6.2015-3677.

[65] *Ansys Workbench User's Guide*, Ansys Inc., 275 Technology Drive, Canonsburg, PA 15317, 2009.

https://dspace.org/

# Wind tunnel installation effects on a high-speed exhaust flow under large blockage

**Tsentis, Spyros; Goulos, Ioannis; Debiasi, Marco; Prince, Simon A.; Pachidis, Vassilios ...**

**2025-09**
American Institute of Aeronautics and Astronautics (AIAA)
https://doi.org/10.2514/1.a36092
Tsentis S, Goulos I, Debiasi M, et al., (2025) Wind tunnel installation effects on a high-speed exhaust flow under large blockage. Journal of Spacecraft and Rockets, Volume 62, Issue 5, September 2025, pp. 1698-1712

Downloaded from a DSpace repository. https://dspace.org/